A Pore-Scale Study of Underground Hydrogen Storage in Porous Media

Department of Physics and Technology

A Master Thesis in Reservoir Physics

By Per-Hilmar Knut van der Hart

UNIVERSITY OF BERGEN

November 2021

Abstract

With recent global incentives such as the United Nation's Sustainable Development Goals and Glasgow Climate Change Conference, the need for clean energy is at an all-time high. As a green energy carrier, hydrogen is regarded a key factor in the energy transition and a way of decarbonizing natural gas and storing excess energy production from renewables. In 2021, Europe has seen large fluctuations in electricity prices and a rise in demand for temporary energy storage. With seasonal variations in wind, precipitation, and sunlight, the electricity produced from renewables remains unpredictable. The excess electricity during peak production can be used to produce green hydrogen, injected into a subsurface reservoir, and withdrawn at times of high demand. This study focuses on understanding the pore-scale mechanisms and potential of intermittent underground hydrogen storage (UHS) in porous media. In this thesis, pure hydrogen was injected and withdrawn from a distilled water-saturated high-pressure micromodel. Specifically, the experiments were performed to investigate pore-scale observations during one complete cycle of hydrogen injection and withdrawal.

Fifteen experiments with different capillary numbers at 1 and 30 bar pore pressure were conducted during this study. The first ten experiments were focused on the effect of capillary number and pore pressure on fluid saturations, hydrogen trapping, dissolution kinetics, and solubility of hydrogen in water. The remaining experiments investigated individual hydrogen bubbles and clusters to study the effect of different conditions on individual depletion rates, solubility concentration, and types of dissolution.

The influence of capillary number was seen on fluid saturations, trapping mechanism, and dissolution: an increase in capillary number resulted in a higher hydrogen saturation after drainage, mostly I2 snap-off of the hydrogen phase, and increased dissolution and depletion rates. As the pressure increased from 1 to 30 bar, the solubility of hydrogen in water increased, and dissolution and depletion rates increased further. Dissolution occurred primarily through advection of hydrogen by the water phase during imbibition. A small amount of dissolution by diffusion was observed at the lowest capillary number during the initial imbibition period. Individual hydrogen bubbles and clusters were mostly trapped at the roughness of pore walls, which resulted in predominantly heterogenous dissolutions during this study. Homogeneous dissolution was exclusively observed at the lowest capillary numbers due to the transverse water-flow phenomena of an over-saturated micromodel. Individual depletion rates of hydrogen

bubbles were influenced by the available water-hydrogen interface, capillary numbers, and pressure difference. Under various experimental conditions, equilibrium solubility was never achieved because of the limited water-hydrogen interface available for advection and limited resident time.

Acknowledgments

First of all, I would like to thank my supervisor Professor Martin Fernø for giving me the opportunity to work on this new and exciting research project. Thank you, Martin, for the feedback and guidance throughout this final, and most important, year of my studies at the University of Bergen. Without your passion for the energy transition, this, and many other projects would not have been possible.

A special thanks to Ph.D. student Maksim Lyysy for the construction of the experimental setup and assistance in the laboratory. The many discussions we had on the qualitative data of the experiments were of great importance and inspiration for this master's thesis.

Further, I would like to thank my fellow students for a productive and friendly work environment. The breaks with you in between writing always improved my mood and motivation, and the office would not have been the same without you. A special shoutout to Celine Solstad for her feedback and constructive criticism during the final days of my master's thesis.

Finally, I would like to thank my parents Kristian and Cornelia, and sister Solveig. Thank you for your support and for always believing in me.

Bergen, November 2021

Knut van der Hart

Table of Contents

Introduction

In 2015 the United Nations General Assembly created 17 sustainable development goals (SDGs) in response to the "below 1.5 degrees"-target of the Paris Climate Accord. These goals were designed to be "a blueprint to achieve a better and sustainable future for all" (United Nations General Assembly, 2015). One of the most demanding goals set is to have affordable and clean energy for all by 2050 (SDG7). As technology advances and the global population increases, as will the energy demand. There exist different theories and opinions on how SDG7 can be achieved, but one thing they have in common is that there is not one single solution but rather many factors that will contribute to supply the world's future energy demand, while at the same time reduce greenhouse gas emissions.

Hydrogen (H_2), in addition to Carbon Capture and Storage (CCS), increased renewables, biomass and nuclear power will be crucial to fight climate change. Hydrogen may not only act as a future energy carrier, but also as a way of decarbonizing natural gas and ultimately replace fossil fuels in hard-to-abate sectors such as aviation, shipping, and road freight. Electric-powered cars are expected to take over combustion engines in the next 10-15 years (Rowlat, 2021), but the weight of batteries needed for heavy transportation and aviation would far exceed its payload. However, if hydrogen can be safely stored, it can be combusted and combined in chemical reactions with a similar energy output as oil, gas, or coal (Katsutoshi Ono, 2014). A major challenge with hydrogen is its low natural abundance: hydrogen is only found naturally on Earth in small quantities and thus must be produced from another energy source (most frequently either from fossil fuels or through electrolysis of water). Another obstacle to widespread hydrogen usage is, that it needs to be kept at high pressure and low temperature for safe transportation. Because both storage and production demand an energy input, the hydrogen-production source dictates whether it can be considered a clean energy carrier,

In 2018, over 95% of the produced hydrogen came from fossil fuels (IRENA, 2018). There are several available technologies to produce hydrogen from fossil sources. For natural gas, one such method is called *steam methane reforming* (SMR): natural gas is heated several times with water vapor to produce a mixture of hydrogen, carbon monoxide (CO), and carbon dioxide (CO_2). If the produced CO_2 is released into the atmosphere, hydrogen from this process is referred to as grey hydrogen (see Figure 1). If, however, the biproduct CO_2 is captured, transported, and infinitely stored safely underground in a depleted reservoir (in a process called

CCS), the hydrogen is referred to as blue. Another alternative is electrolysis through renewable energy (referred to as green hydrogen) during periods of low-priced electricity and a high percentage of renewables from the total electricity production. (The World Of Hydrogen, 2021).
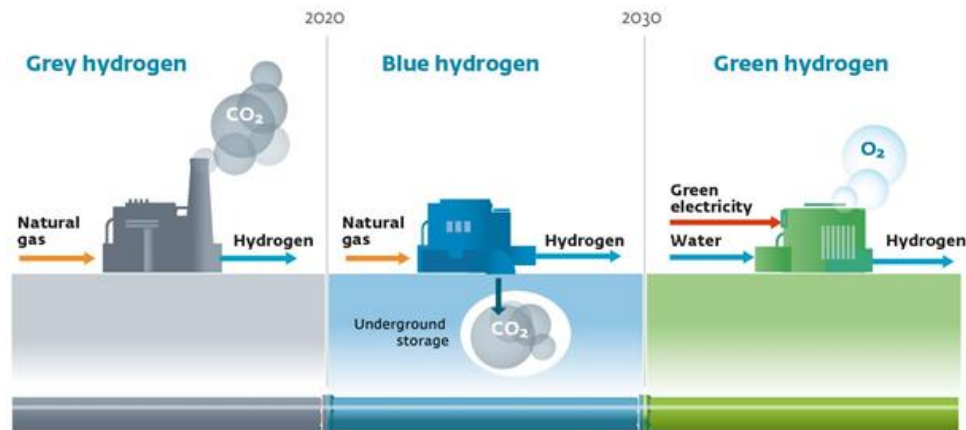

Figure 1. Different hydrogen production sources and CO$_2$ footprints (The World Of Hydrogen).

Renewable energy is often unpredictable and unevenly distributed throughout the year, with high production from hydropower plants during rainy months, or wind parks that depend on daily weather conditions. These fluctuations in energy production result in an uneven electricity price in countries that heavily rely on renewable energy. A solution to this problem would be to use the excess electricity during peak production to produce green hydrogen from electrolysis and store it underground for later usage in periods of low energy production. This approach would make renewable energy predictable and thus also make it more attractive for potential new investors.

Due to a current global gas shortage, Europe is preparing for a cold winter with high gas- and electricity prices (Deutsche Welle, 2021). Hydrogen can be used as a buffer to produce electricity or injected directly into the gas grid as a natural gas substitute during this period of energy insufficiency (Bruun, Graf, Iskov, & Koch, 2014). Norway has already seen an increase in its electricity prices because of the dry summer and fall of 2021. Approximately 90% of Norway's 153 TWh annual electricity demand is covered by its hydropower plants (NVE, 2021). Because of its climate, the energy consumption of Norway has periods where it is inversely proportional with water inflow into the basins of its hydropower plants (see Figure

2). This inverse proportionality is due to most of the water basins being filled during Norway's warmer spring months when the snow is melting. The electricity demand however is highest during the colder winter months, when there is less rain and most of the precipitation is in form of snow (Dannevig & Harstveit, 2021). During weeks 3-5 and 23-41 (green area) Norway's hydropower production exceeded its energy consumption, which could have been used to produce and store green hydrogen for later usage during energy shortage (red area; weeks 1-3, 5-19 & 47-52). These periods would correspond to a storage duration of a minimum of 42 to a maximum of 133 days of temporary hydrogen storage.
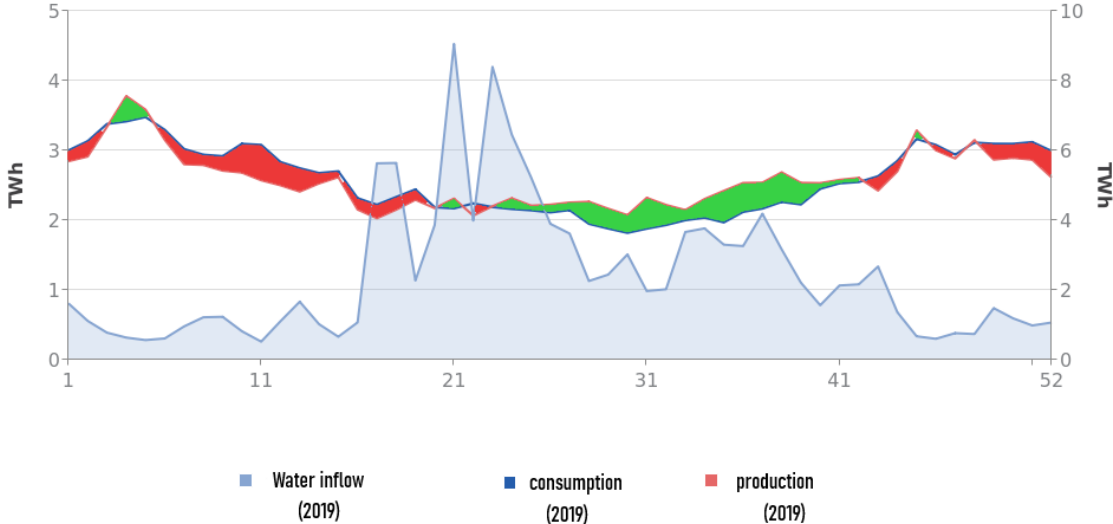
Figure 2. Norway's hydropower energy production and total energy consumption in 2019 (NVE). The green area shows periods where production exceeds consumption, while red indicates the opposite.

In regards to underground energy storage, one of the most effective and inexpensive ways to store hydrogen is to inject it into a geological formation with existing infrastructure like a depleted gas reservoir, salt caverns, or aquifers (Azretovna Abukova, Nabievich Zakirov, Pavlovich Anikeev, & Sumbatovich Zakirov, 2020) (see Figure 3). Underground hydrogen storage experience is scarce and the only pure hydrogen that has been stored is in salt caverns in Texas, USA, and Teesside, UK (Pfeiffer, Beyer, & Bauer, 2017). Experience with hydrogen storage in porous media is even less: the few cases where hydrogen has been injected into a porous geological formation are as town gas, a mixture of hydrogen with other gases such as

methane, carbon monoxide, and nitrogen (N_2) (Amigáň et al., 1990). In France, Engie (former Gaz de France) operated an underground storage facility in a depleted aquifer dome just outside Paris. Town gas containing over 50% hydrogen was stored there from 1957 to 1974, and over 150 million m^3 of hydrogen was injected during this period. Afterward, studies conducted showed no traces of hydrogen in the groundwater from that area, indicating low or no contamination by the stored hydrogen (Azretovna Abukova et al., 2020). To reduce costs, CO_2 and N_2 have been discussed as cushion gas alternatives to hydrogen (Pfeiffer et al., 2017). While the usage of these inert gases is cheaper, it will also increase the risk of contaminating pure hydrogen. However, the impact N_2 has on the combustion characteristics of hydrogen-rich synthetic gas in gas turbines is relatively low (Lee, Seo, Yoon, Kim, & Yoon, 2012).
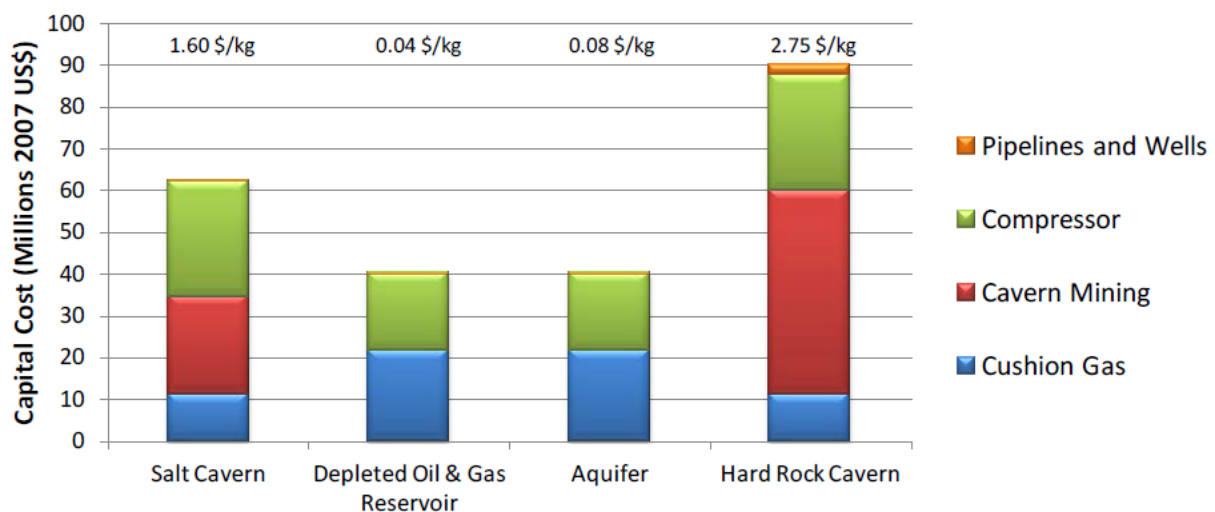
Figure 3. Estimated capital costs per kg hydrogen for different underground storage alternatives and their source of expenses (Lord, Kobos, Klise, & Borns, 2011).

Similar to UHS, micro-scale experiments with pure hydrogen have been few, thus, some inspiration for this master thesis came from CO_2-experiments, especially by Buchgraber et al. (2012) and Chang et al. (2016). Historically, experiments with natural gas or CO_2 storage have been used analog to hydrogen storage (Carden & Paterson, 1979). Although there are significant dissimilarities when using hydrogen, due to corrosion on the equipment as well as potential effects on well and formation integrity (Pfeiffer et al., 2017). Another important difference and potential advantage is that due to its stable viscosity, hydrogen shows little difference in relative permeability and capillary pressure when varying temperature and pressure conditions. In contrast, CO_2 strongly varies with pressure and temperature when paired with other fluids

(Yekta, Manceau, Gaboreau, Pichavant, & Audigane, 2018). Thus, although hydrogen experiments for this master thesis have been conducted similar to natural gas and CO_2, results will vary and should be discussed and compared as a guideline, not benchmark.

1 Theory

This chapter provides insight into the physical and chemical aspects of underground hydrogen storage (UHS). Section 1.1 describes the general theory of a two-phase flow inside a porous media, whereas 1.2 illustrates the specific mechanics behind a complete UHS cycle.

1.1 General theory

1.1.1 Wettability

In a porous media where two or more immiscible fluids are present, the media's wettability is defined as "[…]the tendency of one fluid to spread on, or adhere to, the solid's surface in the presence of another immiscible fluid." (Zolotuchin, 2000). When water spreads on the surface, the media is defined as being *water-wet*. The opposite, when oil preferentially spreads on it, is known as *oil-wet*. When the media prefers neither oil nor water, it is defined as *neutral*-wet. As seen in Figure 1.1, one way of determining the wettability is to measure the contact angle between the densest fluid and the solid's surface.
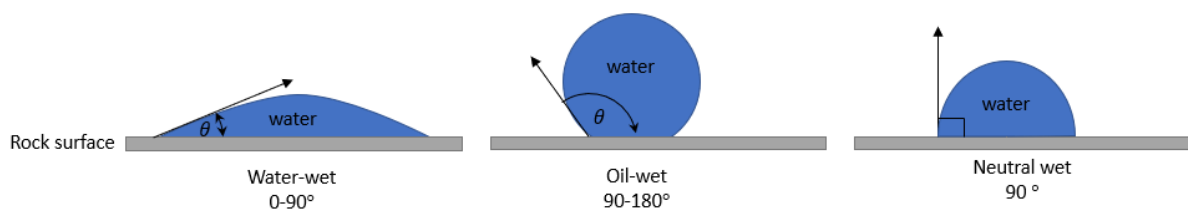
Figure 1.1. Contact angles and their representative wettabilities (Sandnes, 2020).

For a gas-liquid system, a way of measuring wettability is by the *captive bubble method* (Jiang, Li, & Zhang, 2013). Because gas usually is less dense than a liquid, the solid is used as a ceiling to capture the bubble (as seen in Figure 1.2), and the gas contact angle (θ_g) between the gas and the solid is measured. Table 1.1 shows criteria for different wettabilities based on θ_g.
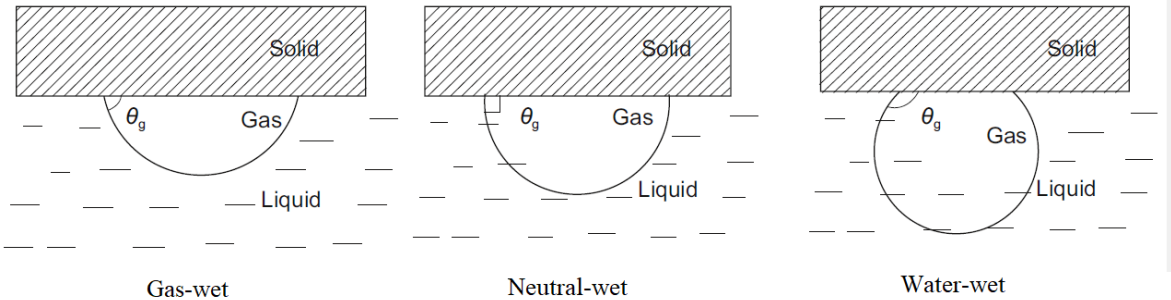
Figure 1.2. Wettability based on the contact angle between a gas and a solid surface in presence of a liquid (modified from Jiang et al.).

Table 1.1. Gas wettability based on the measured gas-solid contact angle.

Gas contact angle θ_g [˚]	Gas Wettability
[0, 90)	Gas-wet
90	Neutral-wet
(90,180]	Water-wet

Wettability is an important factor of a porous media as it influences the fluid saturation and distribution, as well as capillary pressure and potential recovery of the injected fluid at a later stage.

1.1.2 Capillary pressure

In the presence of two immiscible fluids, the capillary pressure (P_c) is the amount of pressure required by the non-wetting phase to displace the wetting phase inside a porous media. In a water-wet system, capillary pressure is defined as:

$$P_c = P_{nw} - P_w \qquad (1.1)$$

where P_c is the capillary pressure, and P_{nw} and P_w are the pressures of the non-wetting and wetting phase, respectively. The interface of two immiscible fluids in a narrow cylindrical tube will usually be curved in a form of a meniscus. Thus, Laplace suggested a relation for capillary pressure of two immiscible fluids as followed:

$$P_c = \sigma \left(\frac{1}{R_1} + \frac{1}{R_2} \right) \qquad (1.2)$$

where σ is the interfacial tension [nM/m] between the wetting and the non-wetting fluid, and R_1 and R_2 are the radii of the interface curvature. For a spherical droplet, the simplification of $R_1 = R_2 = r$ can be made (Zolotuchin, 2000). This results in what is known as the Young-Laplace equation for capillary pressure:

$$P_c = \frac{2\sigma cos\theta}{r} \qquad (1.3)$$

where θ is the wetting angle [°] described in section 1.1.1.

Historically, P_c has been of great importance in petroleum-related studies, and P_c concepts have been used to evaluate rock quality, pore size distribution, and fluid saturations of a reservoir.

1.1.3 Capillary number and fluid saturations

When injecting a fluid into a porous media with a native fluid present, two forces are opposed each other: the viscous force driving the injected fluid, and the local capillary forces holding the native fluid in place inside the pores (see section 1.1.2). The ratio of these forces is known as the capillary number (N_c) (Zolotuchin, 2000) and one of the definitions by Lien et. al (2004) is:

$$N_c = \frac{u_d \mu_n}{\sigma} \tag{1.4}$$

where u_d is the Darcy velocity of the injected fluid [m/s], μ_n is the viscosity of the native fluid [pascal seconds] and σ [mN/m] is the interfacial tension between the injected and native fluid. Generally, N_c has been used as a guideline to increase the production of the native fluid (i.e.: gas or oil), leaving only the minimum, known as the residual saturation, behind. This is done by either decreasing the interfacial tension or increasing the viscosity and Darcy velocity. The Darcy velocity is defined as:

$$u_v = \frac{Q}{A} \tag{1.5}$$

where Q is the injection rate [mL/h] and A is the cross-section [µm] of the pore. Because both interfacial tension and viscosity vary with pressure, as well as the Darcy velocity being a function of Q, N_c has also been used as a way to compare experiments under different conditions.

1.1.4   Hysteresis

The definition of hysteresis varies from field to field, but a generalization is that is defined as the change of the state of a system depending on its history (Saga, 2021). For a two-phase immiscible flow in a porous media, the two important hystereses are the wetting-angle and capillary hysteresis.

Experiments have shown that when gas moves into pores occupied by water, the wetting angle is different than when water displaces gas in the same pore space. This phenomenon shows a memory of the system and is known as *wetting angle hysteresis* (Zolotuchin, 2000). A way to quantify this phenomenon is to measure the advancing angle θ_a when gas is displacing water and the receding angle θ_r when gas is being displaced by water.

As a fluid is injected into a porous media, the media's wettability and original fluid saturation define the nature of the process. In a *drainage* process, gas is injected into a water-wet porous media with native water present. In this case, the non-wetting phase (gas) is displacing the wetting phase (water) (Lien, 2004). When reinjecting water into the media, the wetting phase displaces the non-wetting phase in a process called *imbibition*. As seen in Figure 1.3, the saturation of the wetting phase does not follow the same path through these processes. This inconsistency of the P_c conditions is known as *capillary hysteresis.*
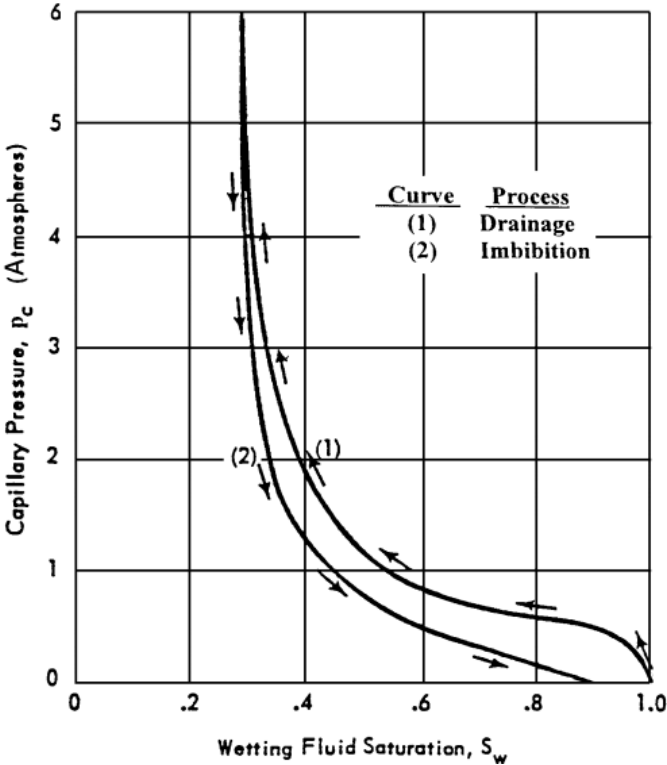
Figure 1.3. A cycle of drainage (1) and imbibition (2) into a porous media. The difference in the drainage starting saturation ($S_w = 1.0$) and imbibition endpoint saturation ($S_w \approx 0.9$) shows capillary hysteresis (Dr.Jawad.Alassal, Yahya Jirjees, Mohamedali, Sajad, & Namiq, 2017).

1.2 Underground hydrogen storage

1.2.1 Drainage and imbibition

Due to the P_c inconsistency discussed in the previous section, drainage must also be categorized differently, depending on the type of porous media: an aquifer has, to the best of our knowledge, only held freshwater or brine during its existence. Thus, initial gas injection into an aquifer is therefore classified as primary drainage (PD). In a depleted oil or gas reservoir, PD occurred millions of years ago when hydrocarbons first migrated into the reservoir (Marshak, 2011). When reinjecting gas into a reservoir with hydrocarbons present, drainage is defined as secondary (SD) or tertiary drainage (TD). Due to capillary hysteresis that may occur during SD and TD, it is therefore important to identify the initial state of the reservoir before fluid injection (Tweheyo, Talukdar, & Torsæter, 2001).

Although commonly referred to as just *imbibition* instead of *primary imbibition*, the same hysteresis also applies to any imbibition process. Both drainage and imbibition have been used to discuss the properties of a reservoir and fluids present. A capillary desaturation curve (CDC) shows the relationship between residual fluid saturation and capillary number. Historically, the CDC has been used in oil recovery to show which flow conditions are required for optimal oil displacement (Yeganeh et al., 2016). Additionally, a CDC can be used to characterize wettability and pore size distribution: in an oil-wet system, the reservoir's response to a given water injection rate would be less favorable, leaving a higher amount of gas behind than it would in a neutral or water-wet system. This is due to the pore network preferring gas rather than water, and thus a higher pressure of the injected water is needed to displace the gas. This can be observed in Figure 1.4: at $N_c = 10^{-3}$, the saturation of the non-wetting phase is reduced from roughly 26% to 10%, while the wetting phase has not been reduced at all. Additionally, $N_c = 10^{-3}$ is also the critical N_c of the wetting phase, meaning this N_c has to be exceeded to achieve any saturation reduction of the wetting phase. The non-wetting critical N_c, however, is between 2-3 orders of magnitudes lower than for the wetting phase. This also shows that at very low N_c (Figure 1.4: $N_c < 10^{-5}$), gas might never penetrate the pore network and the gas saturation in the reservoir will remain at 0%.

A CDC can also be utilized to specify pore size distribution. A steep graph, i.e., when the system goes from a high to a low residual saturation over a narrow N_c, is a sign of a small pore size distribution (see slope of wetting phase Figure 1.4). If the graph has a gentle slope, it shows

that there were pores that were invaded at different pressure regimes, thus indicating a larger variety of pores with different entry pressures (see slope of non-wetting phase Figure 1.4). Small pore size distribution is usually associated with a *homogeneous* reservoir, whereas a *heterogeneous* reservoir contains pores of different sizes and lengths.
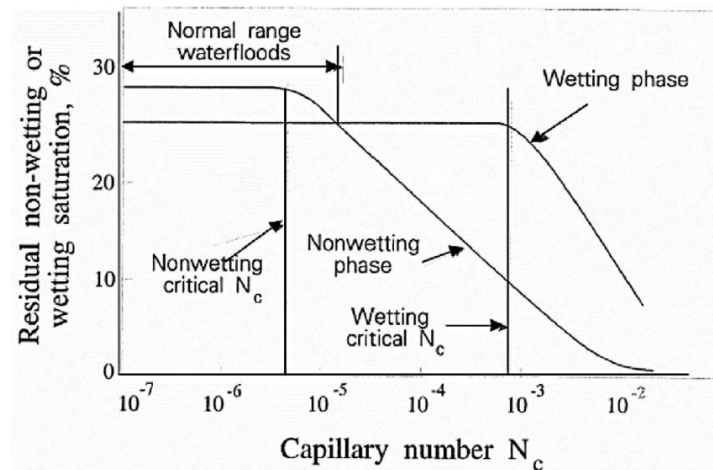
Figure 1.4. Capillary desaturation curve with respect to wettability (Mohsenatabar Firozjaii, Derakhshan, & Shadizadeh, 2018).

1.2.2   Trapping mechanisms

An important aspect of hydrogen storage and extraction is the round-trip efficiency or how much hydrogen is lost during one or more cycles of injection and withdrawal. Different mechanisms will result in trapping and/or immobilization of hydrogen gas when it is injected into a formation occupied by a native fluid. For aquifers, the native fluid is brine, while for depleted reservoirs it can be a mix of brine, gas, and oil. To maximize the storage potential and round-trip efficiency, it is vital to understand these mechanisms and be able to identify the potential actions that may be taken to mitigate losses.

1.2.3 Snap-off

When gas is moving inside a water-wet system, the interfacial forces are such that a portion of the gas may snap-off and separate into a droplet. For a snap-off to occur, the capillary pressure first has to be high enough for the gas to invade the pore, then drop about a factor of two for the water to retake the pore at a later stage (Rossen, 2000). In detail, the gas can only invade the pore if capillary pressure exceeds the capillary entry pressure (P_c^e) of the pore throat. In a water-wet system ($\theta = 0$) with cylindrical pores, equation (1.3) can be simplified as:

$$P_c^e = \frac{2\sigma}{r} \tag{1.6}$$

where σ is the gas-water interfacial tension [mN/m] and r is the radius of the pore throat [µm], thus giving the capillary entry pressure the unit of newton per square meter or [pascal] (Pa) in SI-units. Equation 1.6 states that narrow pores with smaller radii require a larger pressure from the injected phase than bigger pores with larger radii.

Lenormand et al. (1984) were among the first to investigate two-phase immiscible flow under different capillary numbers and characterized the pore-scale mechanisms during imbibition as piston-type movement, IN-type imbibition, and snap-off (see Figure 1.5). During a stable displacement of the non-wetting fluid by the wetting fluid, the non-wetting phase is retreating in a piston-like motion. This motion is also commonly referred to as *sweep out* (Buchgraber, Kovscek, & Castanier, 2012). During IN-type imbibition, the non-wetting phase is either retreating into one pore (I1) or two adjacent pores (I2). Depending on the configuration of the pore network, both events may lead to snap-off and immobilization of the non-wetting fluid.
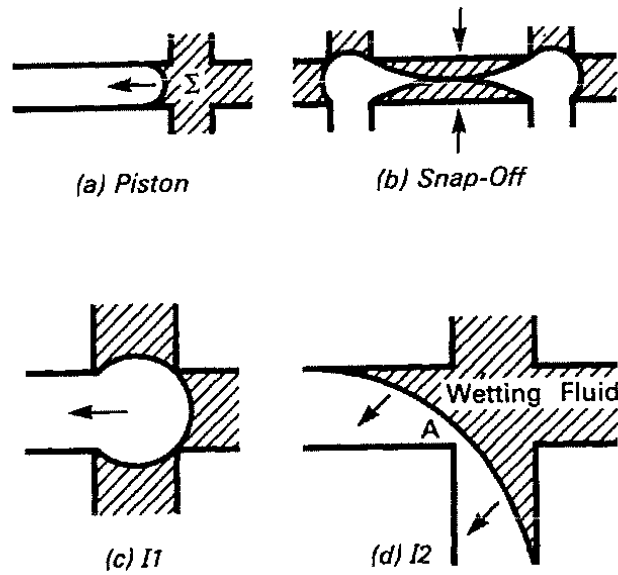
Figure 1.5. Pore-scale view of the different mechanisms that might occur during imbibition (Lenormand & Zarcone, 1984).

1.2.4   Capillary trapping

Once discontinuous, hydrogen gas is capillary trapped. A hydrogen bubble that occupies a large pore cannot move through a narrow pore throat because the capillary entry pressure increases with smaller radii (Buchgraber et al., 2012). Thus, during imbibition, water will choose larger pores with lower resisting pressure and bypass the immobile hydrogen bubbles. The amount of capillary trapped and bypassed hydrogen is related to capillary numbers: for higher N_c, the injected water phase has high pressure and can retake a wider variety of pores that were invaded by hydrogen during drainage (see equation 1.6). At lower N_c, only the largest pores may be retaken. Figure 1.6 shows a capillary trapped hydrogen bubble during water injection. The capillary pressures P_{c1} and P_{c2} are preventing the hydrogen from getting pushed through the pore necks by the viscous force (F_v), thus: $P_{c1} + P_{c2} > F_v$. Due to the difference in radius of the pores surrounding the hydrogen bubble, the capillary force $P_{c2} > P_{c1}$. In theory, there is a third pressure P_{c3} parallel to F_v, but considered negligible due to the large pore radius.
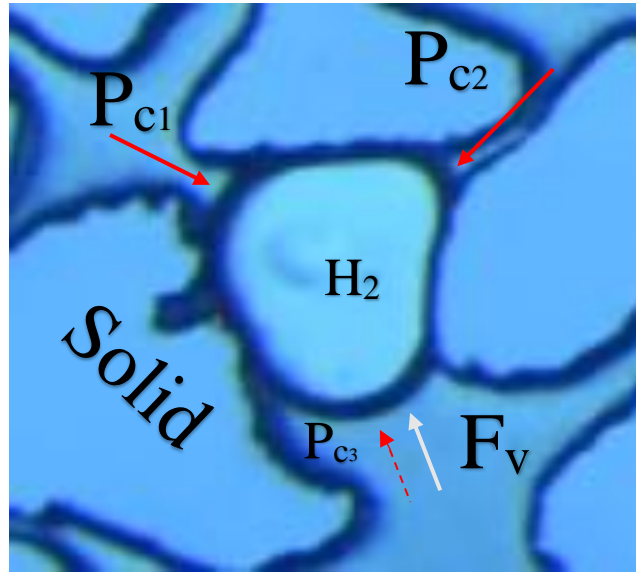
Figure 1.6. Capillary trapped hydrogen bubble during water injection from the bottom. Capillary forces (red arrows) oppose the viscous force (white arrow). $P_{c1} + P_{c2} > F_v$ and $P_{c2} > P_{c1} >> P_{c3}$.

1.2.5   Dissolution and Solubility

After hydrogen is capillary trapped and immobile, there is a contact, or interface, between the hydrogen and the water phase. At an interface where both gas and water are at rest, the dissolution of the gas is expected to be slow (Buchgraber et al., 2012). During this period, dissolution is mainly controlled by the molecular diffusion of dissolved hydrogen in water or the movement from a high concentration to a lower concentration of hydrogen. The law of diffusion can be written in various forms, where the most common is in a molar basis defined as Fick's first law:

$$J = -D\frac{\partial \varphi}{\partial x} \tag{1.7}$$

where J is the diffusion flux measured in the amount of hydrogen that will flow through an area during a unit time interval, D is the diffusion coefficient in area per time, φ is the concentration of hydrogen per volume and x is the position in length. Thus, as the concentration of hydrogen in the water phase increases, the dissolution through diffusion is expected to decrease even

more. During imbibition, the pressure of the injected phase increases, and although originally bypassed, hydrogen will eventually start to mix with water until it is completely dissolved. Throughout this period, hydrogen is contacted by constantly replenished fresh water and dissolution is occurring due to advection in either phase. Because of the increased pressure in the water phase during imbibition, dissolution through advection is partially reversible once the pressure is reduced again. The pressure reduction can either occur when imbibition stops and gas-water equilibrium has been established again, or the solution gas[1] is returned to the original conditions (i.e.: at the outlet/production well) and breaks out of solution as free gas.

Dissolution is also closely related to solubility, which is the property of a substance (solute) to dissolve in another substance (solvent) and is dependent on temperature, pressure, and salinity (see Figure 1.7). Units for solubility may change depending on the study or type of experiment, but the basis remains the same: the ratio of the mass part of solute to mass part of the solvent, usually expressed as [mol/mol] or [mol/kg]. For hydrogen-water (H_2/H_2O) solubility, hydrogen acts as solute and water as solvent. Figure 1.7 shows that the solubility for H_2/H_2O increases with pressure and decreases with higher temperature and salinity in the solvent phase (The Engineering Toolbox, 2021) (Chabab, Théveneau, Coquelet, Corvisier, & Paricaud, 2020). Because water is polar and hydrogen is non-polar, they do not easily form bonds between each other, thus hydrogen is practically insoluble in water at standard conditions (USP, 2015). During experiments, the solubility is often compared to its equilibrium solubility, which is the maximum dissolution under perfect conditions (i.e.: an infinite hydrogen-water interface and instantaneous dissolution everywhere). For equilibrium solubility Chabab et al.'s model can be used:

$$\chi_{H_2}^0 = b_1 PT + \frac{b_2 P}{T} + b_3 P + b_4 P^2 \tag{1.8}$$

Where $\chi_{H_2}^0$ is the solubility of hydrogen in water in mol of hydrogen per kilogram of water, P is the pressure [bar] and T is the temperature [Kelvin]. The empirical coefficients b_1-b_4 can be found in table 7 in *Measurements and predictive models of high-pressure H_2 solubility in brine (H_2O+NaCl) for underground hydrogen storage application* (Chabab et al., 2020). The ratio

---

[1] Hydrogen that has been dissolved in water.

of solubility to its equilibrium is an important factor to be able to see which experimental conditions have the highest effectiveness in regards to dissolution.
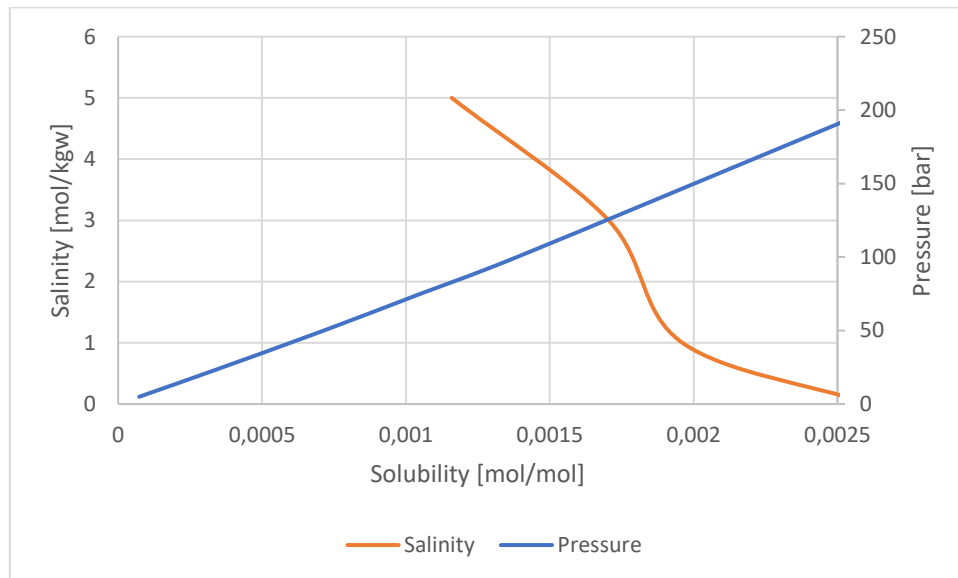
Figure 1.7. How solubility for hydrogen in water changes with respect to pressure and salinity. Units for salinity (m) are mol NaCl per kg of water. Change in solubility for different pressures was measured at $T = 298.15\ Kelvin\ and\ m = 0\ mol/kgw$, and $T = 298.15\ Kelvin\ and\ P = 200\ bar$ for different salinities. Data was collected from Chabab et al. (2020).

For an efficient UHS, both hydrogen-trapping and dissolution are undesirable and need to be kept at a minimum. For a complete cycle of UHS, the physical and chemical aspects discussed in 1.2 are all interconnected in such a way that for a dissolution to occur after hydrogen drainage, there first needs to be a disconnection of the continuous hydrogen phase during imbibition through either I1 or I2 snap-off. Although the pressure of the hydrogen phase increases during imbibition, once the hydrogen is disconnected, the bubbles are capillary trapped, cannot be produced under these conditions, and are thus bypassed. After some time, these trapped hydrogen bubbles start to dissolve into the water phase. Depending on the N_c, hydrogen dissolution occurs through diffusion, advection, or both simultaneously and remains dissolved until the pressure is reduced. An increased solubility, which may be achieved from a higher water- or reservoir pressure, will result in a faster dissolution and higher depletion rates.

2 Methodology

This chapter describes the equipment used, its specific properties, and how the raw data was obtained and analyzed. For this thesis, pure hydrogen was injected into a micromodel fully saturated with distilled water. A real-life representation of an aquifer has a more complex native fluid composition present (e.g.: brine with different minerals), as well as the injected hydrogen may consist of more gases (N_2, CH_4, or CO_2). It is important to acknowledge that this study will focus on general trends and phenomena that, in combination with other studies or literature, may be applicable and upscaled to real scenarios of UHS.

2.1 Experimental Part

2.1.1 Experimental setup

Experiments were performed in the laboratory at the Department of Physics and Technology at the University of Bergen. The existing experimental setup of Ph.D. student Maksim Lyysy at the Reservoir Physics group was adapted and continued to work with.

Equipment:

- High-pressure micromodel
- Quizix Q5200 Pump System
- 1/16" PEEK (Polyether Ether Ketone) and 1/8" steel tubing
- Aluminum holder
- Nikon SMZ1500 microscope
- Nikon D7100 camera
- Photonic LED F1 Cold Light 5500 K light source

Experimental fluids:

- Hydrogen gas from Nippon Gases
- Distilled water

2.1.2 Experimental design

The experimental setup is illustrated in Figure 2.1: the high-pressure micromodel, indicated by the darker blue color, was placed in the middle of the system and connected to a Quizix Q5200 pump system, consisting of two cylinders that could operate independently of each other. The cylinders were filled with distilled water (A) and hydrogen gas (B). The micromodel and pumps were connected by a combination of 1/16" PEEK and steel tubing, as well as 1/8" steel tubing. For optimized flow, the tubings were connected diagonally in port 3 (distilled water) and port 2 (hydrogen). To be able to flush and clean the micromodel after each experiment, an outlet valve and steel tubing that exited into a sink were connected to port 4. Port 1 was not used during experiments.
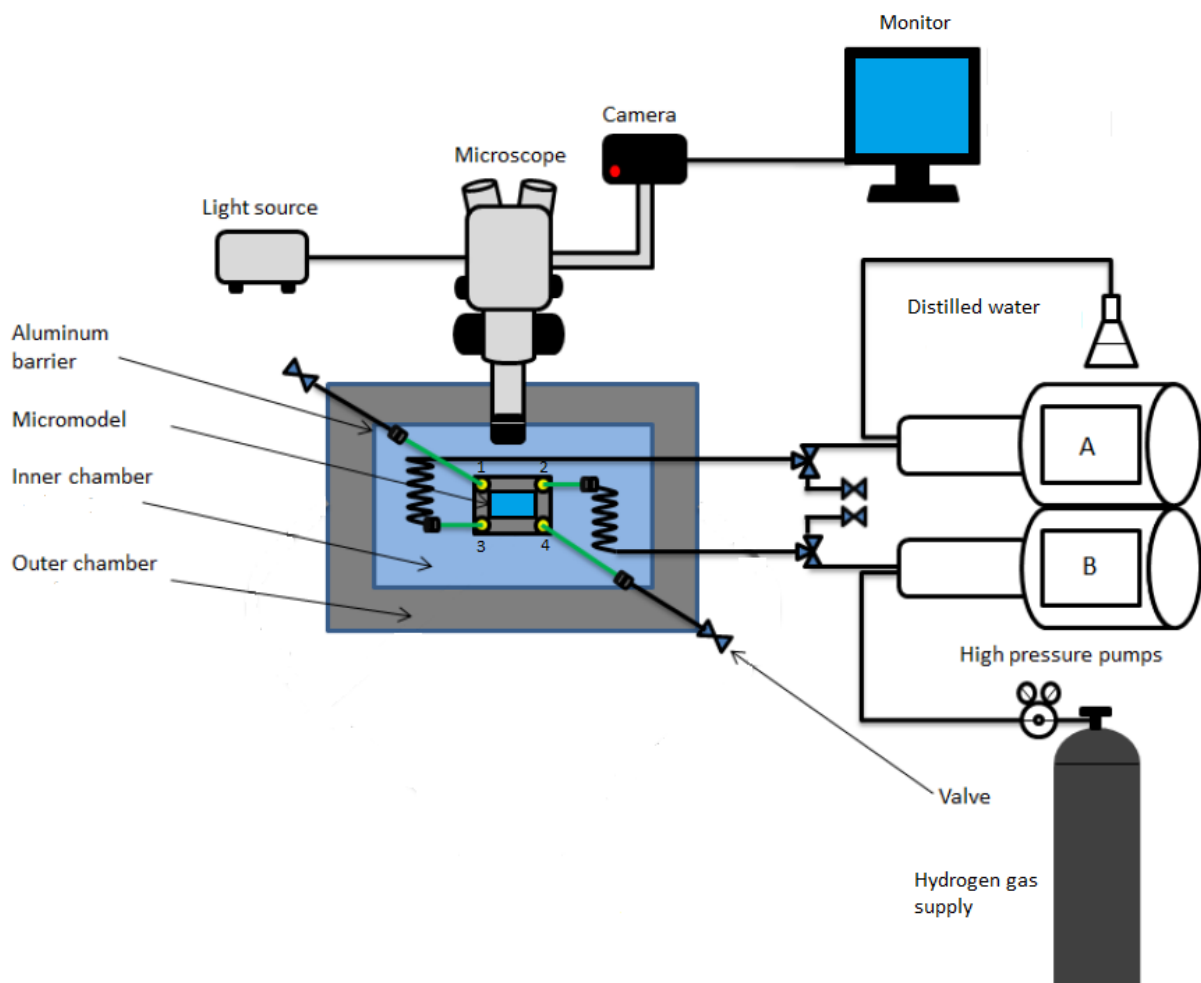
Figure 2.1. Experimental setup (Modified from Iden, 2017).

A camera was mounted on top of a microscope to be able to observe and record drainage and imbibition of the micromodel. To get a better and more detailed image quality, the field of view was illuminated by a concentrated light source. For an improved live observation during experiments, a display was connected to the camera. Each experiment was monitored, either by video or interval pictures and recorded onto the camera's SanDisk memory card.

2.1.3   Micromodel properties

Hydrogen experiments were studied using a 1.7 mm thick micromodel produced by Vrije Universiteit Brussel, which operates at a pressure ranging from 0 to 150 bar. A silicon wafer located at the bottom part of the model was anodically bonded to a borosilicate glass on top, thus avoiding the need for an intermediate layer. The pore network is etched on the silicon wafer by a DRIE (Deep Reactive Ionic Etching) technique to mimic a realistic representation of a heterogeneous porous media found in a reservoir rock. This includes topographical and geometrical rock properties such as roughness of pore walls, sharp corners, and high aspect ratio (i.e., ratio of pore body to pore throat). Specifically, this model is based on a natural sandstone, with an average pore size diameter of 100 µm and an average porosity of $\varphi = 0.6$[2] (Benali, 2019). The pore volume was estimated to be $V_p = 0.01$ mL (Iden, 2017), whereas the absolute permeability was measured to be 3 Darcy. As a result of manufacturing procedures, this micromodel was designed to be of water-wet nature (Buchgraber et al., 2012), which is representable to that of an aquifer. The manufacturer has used the same pattern of pore network a total of 36 times (4 horizontally, 9 vertically) during the production of the micromodel, thus, macroscopically, it is considered homogeneous. Four ports are drilled into the silicon wafer, thus providing an external in- and outlet connection to the micromodel. Two wider channels with a high permeability connect each port and allow fluid flow through the pore network (see Figure 2.2).

---

[2] The average porosity measurement also included the large outer channels which results in an overestimation. For each specific field of view, local porosity should therefore be measured.
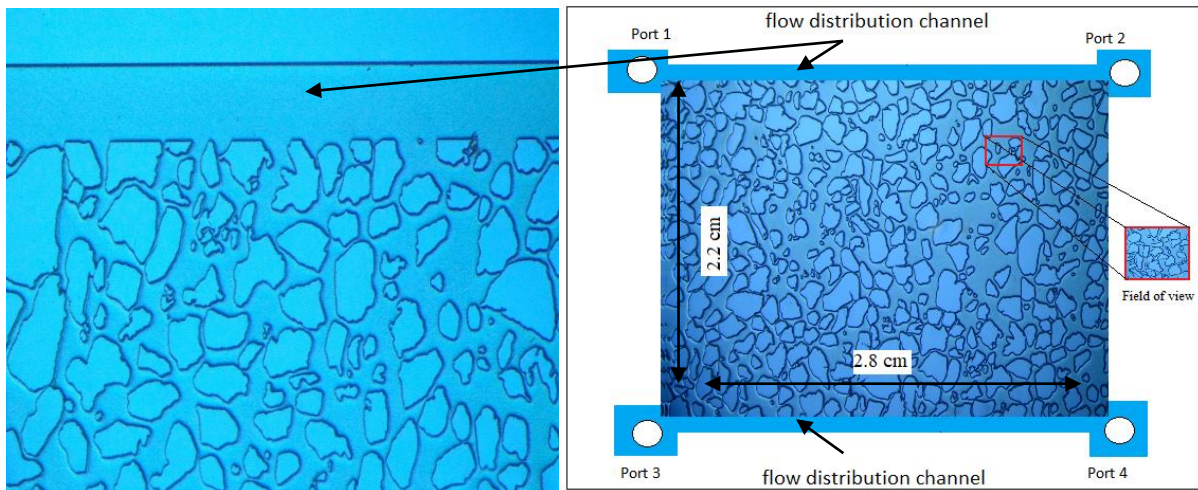
*Figure 2.2. A visual representation of the micromodel, its properties and field of view (**right**), and microscopic view of the micromodel, and one of its outer channels (**left**) (modified from Lysyy).*

A detailed manufacturing description of the silicon wafer micromodel can be found in Hornbrook et al. (Hornbrook, Castanier, & Pettit, 1991).

2.1.4   Experimental procedures

Fifteen drainage and imbibition experiments were conducted to investigate hydrogen saturations, pore-scale trapping mechanisms, and dissolution processes. Each experiment followed the same procedures, including preparations and flushing of the micromodel:

1. Injection pump cylinders A and B were filled with distilled water and hydrogen, respectively.
2. The valve connecting the hydrogen and micromodel was closed, and the hydrogen cylinder was pressurized to the correct experimental pressure.
3. The micromodel was flushed with distilled water and examined carefully to be certain there was no residual hydrogen gas or air in the system.
4. To pressurize the micromodel, the outlet valve was closed, and distilled water was injected until the correct experimental pressure was reached.
5. Once the pressure in the micromodel and hydrogen cylinder were equal, the valve connecting the micromodel and hydrogen was opened.

6. The pump connected to the hydrogen cylinder was set to constant pressure operation mode to maintain the pressure during drainage and imbibition.

7. For drainage, the distilled water pump was set to retract, drawing the hydrogen out of the hydrogen cylinder into the micromodel[3]. For imbibition, the distilled water pump was set to extend, thus injecting water back into the micromodel

8. For drainage: 100 pore volumes (PV) of hydrogen were injected after gas breakthrough. For imbibition: distilled water was injected until all the hydrogen in the micromodel was either swept out or dissolved.

9. For $N_c \leq 7.7 \times 10^{-6}$, the camera was taking interval pictures, whereas for $N_c \geq 7.7 \times 10^{-5}$ the camera was set to video-record mode.

10. After each experiment: to make sure no water got into the hydrogen tubing or cylinder during imbibition, hydrogen was drawn back into the micromodel until gas breakthrough. The hydrogen-micromodel valve was then closed and step 3. was repeated.

A summary of experiments (exp.) and parameters can be found in Table 3.1. Exp. A1-A5 were conducted to investigate trapping mechanisms, hydrogen saturations, dissolution kinetics, solubility, and the change of individual hydrogen bubbles under different N_c. N_c 7.7 $\times 10^{-7}$, 7.7 $\times 10^{-6}$, 7.7×10^{-5}, 1.9×10^{-4} and 3.8×10^{-4} were selected to represent typical conditions of gas withdrawal during water imbibition (Ding & Kantzas, 2007). For a better understanding of diffusive dissolution for ambient groundwater flow[4], an additional rate of 0.01 mL/h was considered but dismissed due to the experimental setup's leakage of between 0.003-0.01 mL/h and thus giving an error margin of 30-100% of experimental values. Exp. B1-B5 were conducted to investigate the effect of pressure on the parameters studied in exp. A1-A5. For $N_c \leq 7.7 \times 10^{-6}$ experiments, the hydrogen saturation after drainage was limited (see Figure 3.3a and 3.3b), thus, these experiments were repeated for a different field of view under exp. A6, A7, B6, and B7. These additional experiments were conducted specifically to investigate individual

---

[3] Due to the compressibility of hydrogen gas, the waterpump was used to control the experiments during both drainage and imbibition.

[4] A regular groundwater flow in an aquifer is roughly $Q = 0.01$ mL/h or $N_c = 4.9 \times 10^{-8}$ (Alley, Reilly, & Franke, 1999).

hydrogen bubbles, where a different field of view did not restrict them from being able to be compared to hydrogen clusters of exp. A3-A5 and B3-B5.

A more in-depth way of looking at dissolution is through depletion rate (Q_d), or how much mass is dissolved per time interval. Hydrogen depletion rates were calculated similarly to Chang et al.'s (2016) experiments with supercritical CO_2, where they measured the change in fluid saturation between two consecutive images to calculate Q_d (Chang et al., 2016). For this master thesis, the VLC media player was used to first divide imbibition videos into frames. For each chosen frame (image), the area of hydrogen was then measured using ImageJ software, and the following equation was used to calculate the depletion rate:

$$Q_d = \frac{\Delta A d \rho}{\Delta t} \qquad (2.1)$$

Where Q_d is the depletion rate [picogram/second], ΔA is the change in the area of hydrogen between two consecutive images [μm^2], d is the depth of the micromodel 30 μm, ρ is the density of hydrogen [gram/milliliter] and Δt is the time [seconds] measured between two consecutive images. In theory, Q_d can be calculated with just two points: between $t = 0$ (just before hydrogen dissolution had started), and $t = t_d$ (when all the hydrogen had been dissolved). The two point-method will give an average Q_d for the whole dissolution process, but for in-depth analysis at pore-scale dissolution and a better understanding of the mechanisms present, a more detailed approach was needed. Thus, in addition to the macroscopic two-point method, individual hydrogen bubbles and clusters have also been analyzed. For these individual depletion rate calculations, between 7-15 points were used that, in combination with video examination, gave a more precise understanding of the pore-scale dissolution processes.

2.2   Image analysis

The raw data was obtained either by screenshots taken from video recordings or images generated by interval picture mode. The two sources of data had different camera settings: 1/30 shutter speed, f/13 aperture, and 1920×1080 resolution for videos; and 1/5 shutter speed, f/13 aperture, and 6000×4000 resolution for images. These settings resulted in different quality of the generated screenshots: video recording had slightly darker images than those obtained by interval picture mode, and the total area of the generated image was 2,073,600 pixels (1920×1080) and 24,000,000 pixels (6000×4000).

For fifteen conducted experiments, approximately 300 images were analyzed and quantified. The main task was to map hydrogen distribution in these images, examine how its saturation and shape changes over time, and if there were any observable trends.

Hydrogen saturations were calculated using the following equation:

$$S_g = \frac{A_h}{A_t \varphi_l}$$ (2.2)

where S_g is the hydrogen saturation, A_h is the area of hydrogen [px], A_t is the total area of the image [px], and φ_l is the local porosity of the chosen field of view. With only water and hydrogen present, by definition, the total fluid saturation in the micromodel is $S_w + S_g = 1$, thus the water saturation is defined as $S_w = 1 - S_g$.

2.2.1   Microscopic view

Most of the experimental work is based on observation through the microscope, it is therefore important to be able to distinguish between the different fluids and media present in the micromodel. Figure 2.3 shows an image of the micromodel after drainage, where hydrogen and distilled water are present. The visual difference of the media observed in the micromodel is caused by their respective refractive indexes. The dimensionless index describes how fast light propagates through a medium and determines how much of the light is bent when entering a

different material (Iden, 2017). Thus, to be able to visually distinguish between different fluids and materials present, they must have a difference in refractive index.

Table 2.1 gives an overview of the different materials present in the micromodel and their respective refractive indexes. Hydrogen, water, and borosilicate glass all have similar indexes with a difference of only 0.33 and 0.18 between hydrogen-water and water-borosilicate, respectively. With the lowest refractive index, hydrogen appears as the brightest fluid on the experimental images. Light propagates slower through water, thus making it appear slightly darker. The black lines surrounding the grains appear to be a shadow caused by the topography of the micromodel.

Table 2.1. Refractive indexes of the different media present in the micromodel.

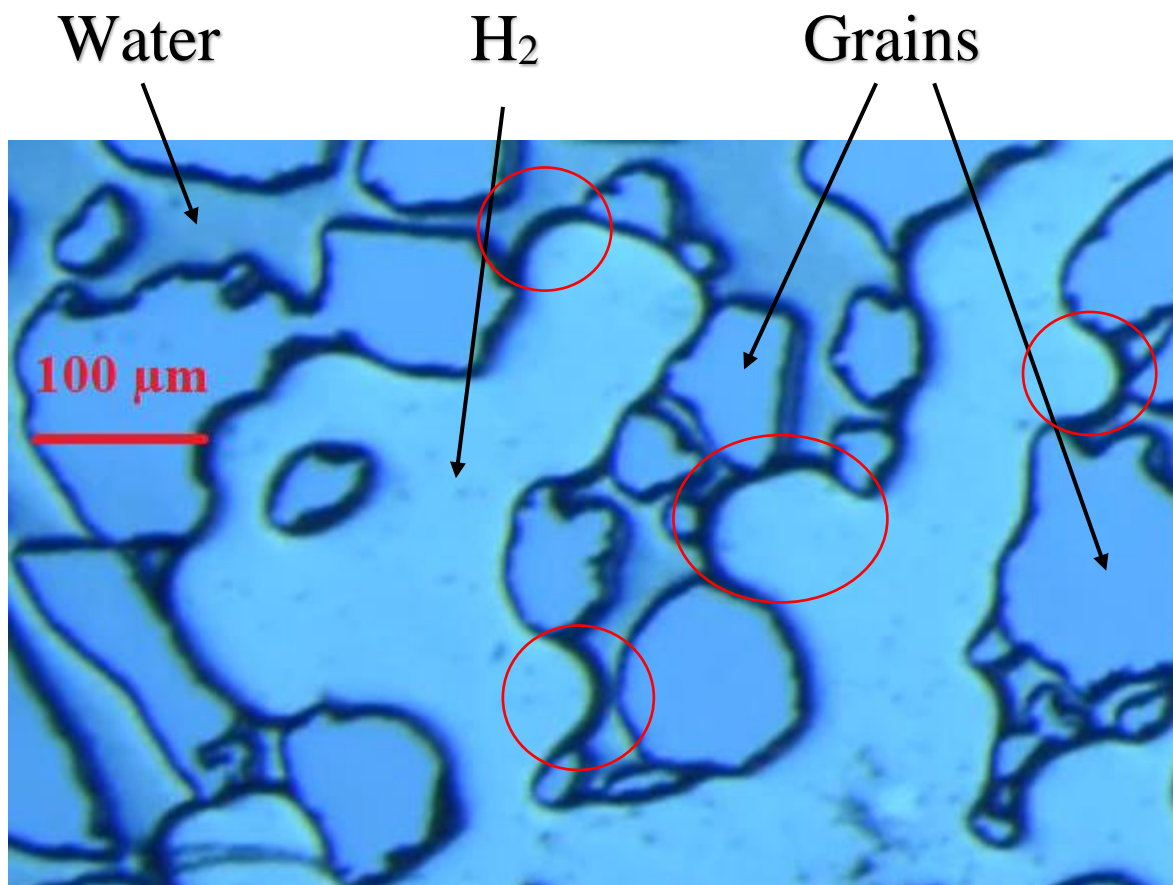| Media	Refractive index n	Reference
Hydrogen gas	1.0001	(Peck & Huang, 1977)
Water	1.3325	(Hale & Querry, 1973)
Borosilicate glass	1.5168	(Polyanskiy, 2021)
Silicon	3.5000	(Jin, Kim, Kang, Kim, & Eom, 2010)

Figure 2.3. Microscopic view of the pore network filled with distilled water and hydrogen. Red circles show examples of the curvature of hydrogen towards the water phase.

Due to the water-wet nature of the micromodel as well as the general immiscibility between the wetting and non-wetting fluid, hydrogen gas will develop a convex curvature toward the water phase and less light will be reflected into the microscope. Thus, contrary to the area surrounding the grains, the black line at the hydrogen-water interface is an absorption of light due to curvature, and not a shadow (Iden, 2017). In addition, because the interface curves vertically (top to bottom), it appears thicker than it actually is and a difference in thickness compared to the shadows of the grains can be observed (see red circles Figure 2.3).

2.2.2   Image editing and optimization

For fluid saturation calculations, the light source illuminating the micromodel was not optimally distributed, which resulted in light gradually diminishing outwards from the center. The difference in luminosity was problematic due to the image analysis software ImageJ depending on differences in color, brightness, and saturation to be able to distinguish between water and hydrogen. Water, hydrogen, and grains all appeared in a blue hue, and although the different

refractive indexes for hydrogen and water make them easily distinguishable to the human eye, ImageJ was not able to do the same (see Figure 2.4b). To bypass this problem, the graphics editor Paint 3-D was used to manually shade the hydrogen in a different color, thus enabling ImageJ to precisely identify the gas in the micromodel. After using the graphics editor, the new color appeared in the color distribution field (red square; upper right corner in Figure 2.4c). ImageJ was then able to identify the new color, measure the area of the pixels that were hydrogen (see yellow outlines in Figure 2.4c), and equation 2.2 was used to calculate the hydrogen saturation for each image.
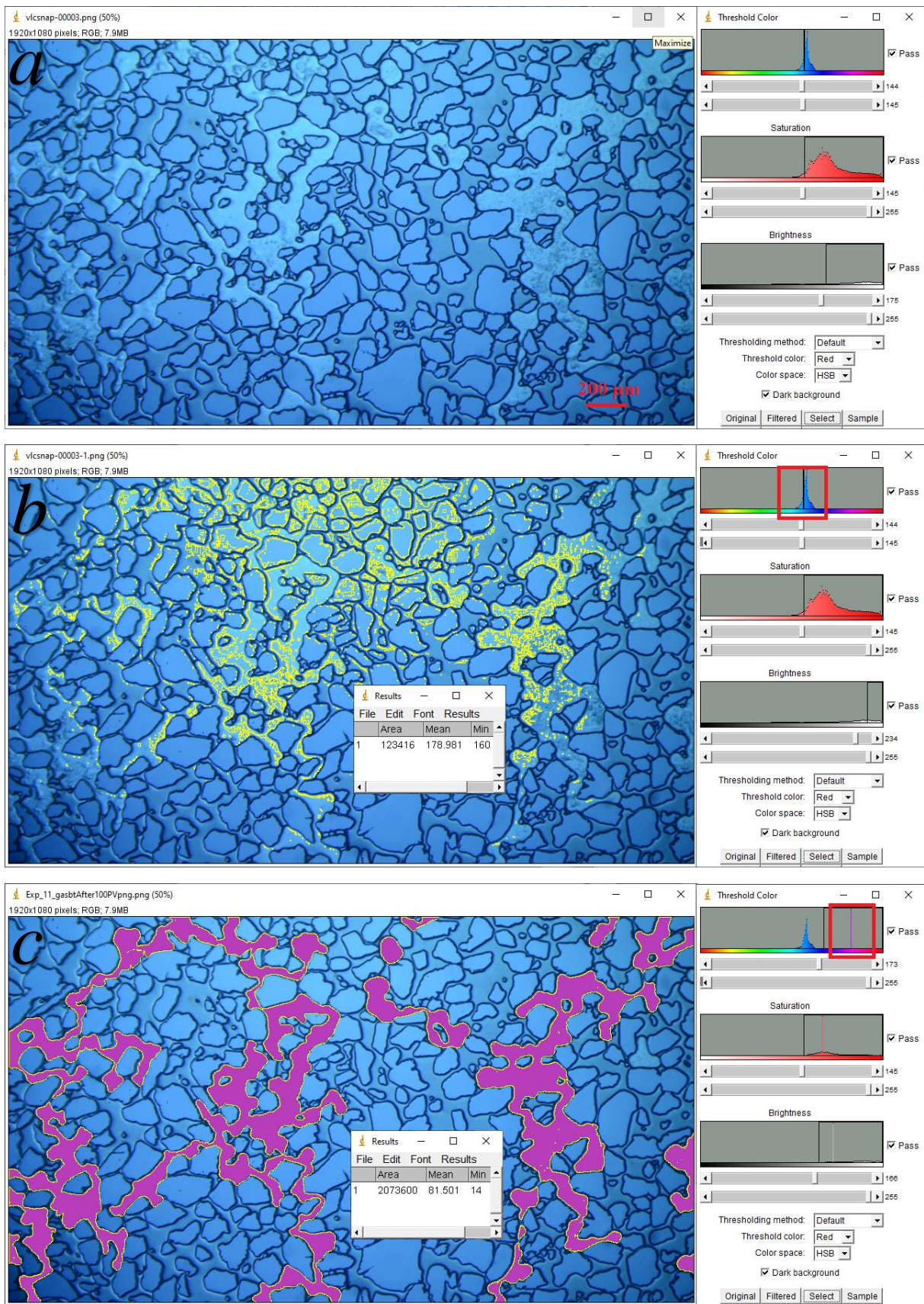
Figure 2.4. Hydrogen mapping using ImageJ. The yellow outlines show the area that has been selected as the area of hydrogen. **a** *Original image with no adjustment.* **b** *Original image with an attempt at color threshold adjustment.* **c** *Paint 3-D-Edited image with successful adjustment.*

Image optimization was the most time-consuming part of this master thesis. Due to the difference in brightness, images from interval picture mode were usually more difficult to optimize than those obtained from video recordings. Thus, depending on the fluid saturation and quality of the picture, one image would take between 10 to 40 minutes of Paint 3-D optimization before Image-J could be used. For approximately 300 images edited during fifteen experiments, the work corresponded to approximately 150 hours alone. Because quantification of video and images is a crucial part of hydrogen analysis in a micromodel, for future work it would be recommended to use dyed water or fluorescent tracers for experiments. This would reduce the work hours significantly, but also increase the accuracy of hydrogen mapping using Image-J directly without the use of extra software such as Paint 3-D.

3 Results and Discussion

This chapter presents the experimental results, with qualitative and quantitative discussion and analysis. Sections 3.1 and 3.2 show some of the micromodel properties such as local porosity and fluid saturations after drainage. Section 3.3 evaluates the trapping mechanisms, dissolution, and solubility of the hydrogen saturation during imbibition, as well as analyzing individual hydrogen bubbles of each experiment. In section 3.4 the round-trip efficiency of UHS and some of the limitations of the micromodel at low N_c are discussed.

3.1 Micromodel properties

3.1.1 Local porosity

To be able to calculate fluid saturations correctly, it was important to measure the local porosity (φ_l) for the specific field of view used during the experiments. Because the average porosity takes the whole micromodel, including the outer flow distribution channels, into account, the total average porosity was overestimated compared to the local porosity. For improved accuracy and results, it was also important to use the same field of view throughout the experiments.

Because the depth is constant throughout the micromodel, instead of the volume, the ratio of the area of the pores to the total area of the field of view was used for calculating φ_l. For improved accuracy, the two following methods were used that, by definition, will give the same result:

- Pore method: The area of the pore network was mapped, measured, and $\varphi_l = \frac{A_p}{A_t}$ was used to determine the local porosity.
- Grain method: The area of each grain was mapped, measured, and $\varphi_l = 1 - \frac{A_g}{A_t}$ was used to determine the local porosity.

where A_t was the total image area [px], and A_p and A_g were the area [px] of the pore network and grains, respectively.

Table 2.2. Local porosity measurements using different methods

Method	Area [px]	Tot. Area [px]	Porosity ±0.01
Grains	133454	2073600	0.36
Pores	743799	2073600	0.36
Average			0.36
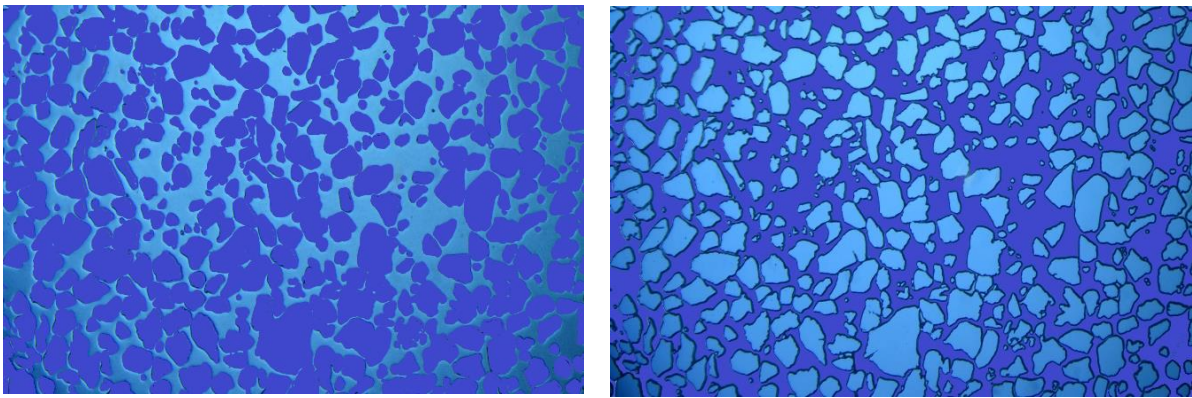
*Figure 3.1. Local porosity calculations where the area of grains (**left**) and pores (**right**) were measured, respectively.*

3.2   Hydrogen gas drainage

This section analyses and discusses the results obtained during or after hydrogen drainage of the water-saturated micromodel at 1 and 30 bar, and $N_c = 7.7 \times 10^{-7}$, 7.7×10^{-6}, 7.7×10^{-5}, 1.9×10^{-4}, and 3.8×10^{-4}. The camera used in the experimental setup was able to record a maximum of 30 minutes before a manual restart. Experiments conducted at $N_c = 7.7 \times 10^{-7}$ took approximately 24 hours to complete and had to be executed overnight, therefore manually restarting the video every 30 minutes was not possible, and interval picture mode was chosen for exp. A1, B1, A6, and B7. The remaining experiments were completed between 10 to 90 minutes, and video recording mode was therefore selected as the observed method. An important assumption that the fluid saturation observed in the chosen field of view could be upscaled to that of the whole micromodel was made. The assumption was based on two premises:

- After 100 PV of hydrogen drainage, the micromodel was expected to be fully saturated with hydrogen to its maximum storage potential[5].
- Due to the repeated pore network, the micromodel was considered macroscopically homogenous.

---

[5] The storage potential is based on theory of wettability, capillary pressure, N_c and fluid saturations discussed in section 1.1

Table 3.1. Summary of drainage and imbibition experiments.

Exp. #	Q [mL/h] ±0.2%	v [m/d] ±0.2%	p [bar] ±0.2%	N_c ±0.3	S_g ±0.02
A1	0.1	4.8	1	7.7×10^{-7}	0.16*
A2	1	47.6	1	7.7×10^{-6}	0.05*
A3	10	476.2	1	7.7×10^{-5}	0.65
A4	25	1190.4	1	1.9×10^{-4}	0.67
A5	50	2381.0	1	3.8×10^{-4}	0.67
B1	0.1	47.6	30	7.8×10^{-7}	0.20*
B2	1	4.76	30	7.8×10^{-6}	0.09*
B3	10	476.2	30	7.7×10^{-5}	0.53
B4	25	1190.4	30	1.9×10^{-4}	0.57
B5	50	2381.0	30	3.9×10^{-4}	0.61
A6	0.1	4.8	1	7.7×10^{-7}	0.05*
A7	1	47.6	1	7.7×10^{-6}	0.09*
B6	0.1	4.8	30	7.8×10^{-7}	0.11*
B7	1	47.6	30	7.8×10^{-6}	0.09*

*The uncertainties for these saturations can be seen in Figure 3.2. ±0.02 applies for the remaining experiments.

For N_c calculations (see equation 1.4), the depth of the micromodel (30 µm) was used as a substitute for the area in equation 1.5. Because the depth is assumed to be constant throughout the micromodel, as well as hydrogen's and water's viscosity and their interfacial tension varying little with increased pressure, the main factor controlling N_c was Q. For easier comparison, N_c were frequently categorized as low-, med- and high-N_c instead of their exact values. These correspond to injection rate values 0.1-1.0 mL/h (low), 10.0-25.0 mL/h (med) and 50.0 mL/h (high).

3.2.1 Fluid saturation and storage capacities

The fluid saturations after drainage indicate the hydrogen storage capacity and general properties of the media. A higher N_c meant the pressure of the hydrogen phase was increased during injection and thus able to penetrate a wider variety of water-filled pores. A lower N_c was able to invade the larger pores where, according to Young-Laplace, the capillary entry pressure was the lowest. For this study, the CDC has been modified to show which N_c gives the lowest water saturation and thus the highest hydrogen storage capacity (see Figure 3.2). The lowest possible water saturation after drainage is defined as the irreducible water saturation (S_{wi}), which is also called immobile water, due to it being trapped and unable to move (or be moved). For a specific system, a water saturation less than S_{wi} cannot be achieved, unless the variables in equation 1.4 are altered (i.e.: changing the wettability or the reduction in interfacial tension by addition of chemicals (Zolotukhin & Ursin, 2000).
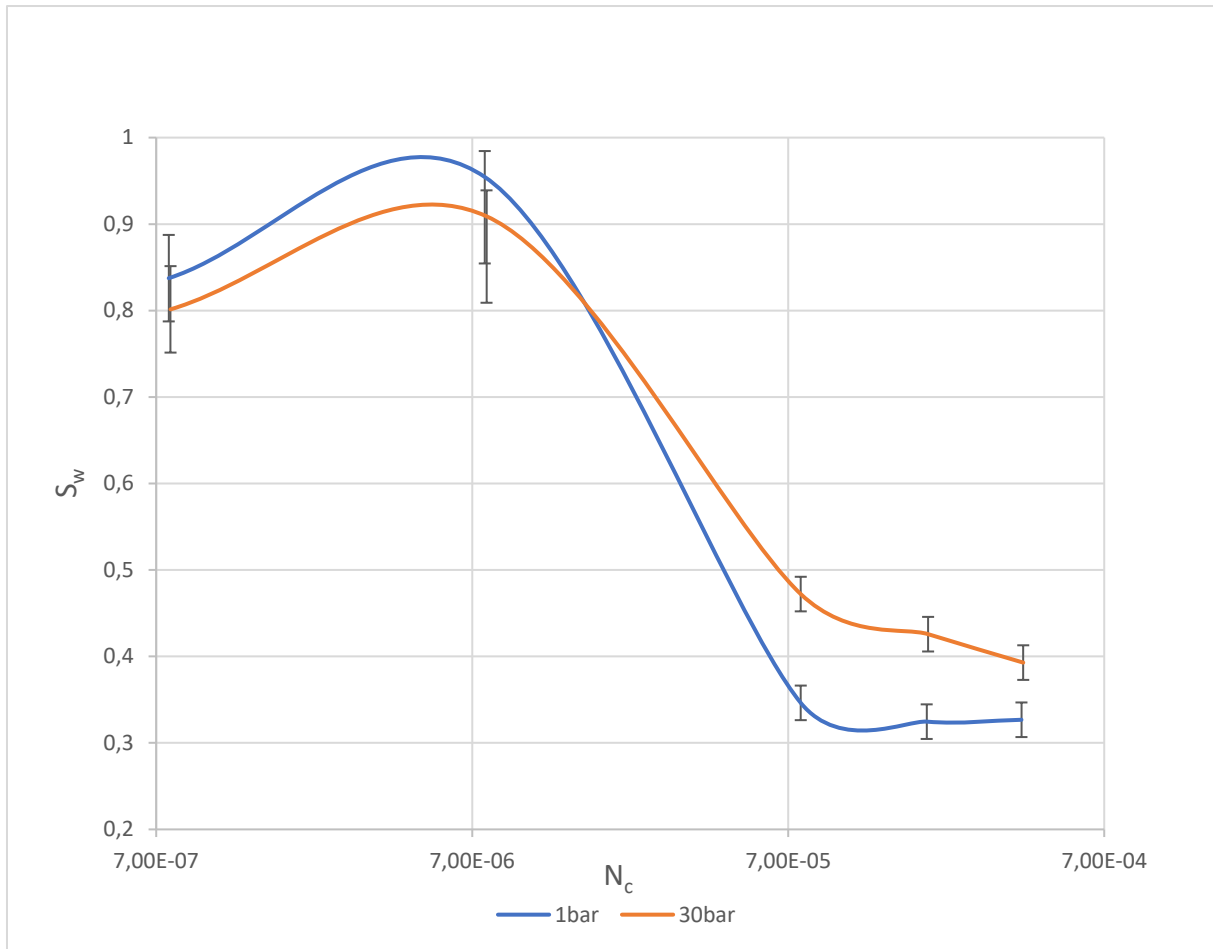
Figure 3.2. Modified Capillary Desaturation Curve for experiments A1-A5 (blue) and B1-B5 (orange). The curve flattens after S_{wi} had been reached.

Throughout every drainage experiment, hydrogen gas breakthrough started from the right side of the field of view where the gas cylinder inlet was located. The lowest achieved hydrogen saturation after PD was 5% during exp. A2 and A6, and the highest was 67% during exp. A4 and A5. An increase in N_c resulted in a higher hydrogen saturation except for exp. A1 and A2, where the saturations were 16% and 5% (Figure 3.3a and 3.3b), and B1 and B2, with $S_g = 20\%$ and $S_g = 9\%$, respectively. The field of view covers about 1% of the total micromodel (Lysyy, 2018), thus when dealing with low N_c, the randomness of the path the hydrogen will take is a factor of uncertainty: hydrogen may break through at a different location in the micromodel for different experiments with identical N_c and pressure. Although the micromodel is cleaned of residual hydrogen after each experiment, this difference can be linked to hysteresis, as well as small deviations in room temperature and pressure. In addition, pore-scale displacement has shown stochastic behavior in porous media (Zhang, 2001). At med-high N_c, the increased pressure of the hydrogen phase could penetrate a much larger variety of pores, thus randomness

of the path taken and stochasticity is decreased significantly. Hydrogen saturations at low N_c were, therefore, less accurate than at med-high N_c. This was confirmed at a later stage when experiments for $N_c \leq 7.7 \times 10^{-6}$ were repeated during exp. A6, A7, B6 & B7, and S_g after PD were 5%, 9%, 11%, and 9%, sequentially[6]. For low N_c, the repeated experiments show better compliance with the theory behind CDCs and capillary numbers than the initial experiments. More importantly, though, it highlights the increased uncertainty for these conditions: for identical experimental conditions, S_g was over three times higher for A1 than A6, and almost two times higher for B1 than B6.

Because the hydrogen saturations for all experiments at $N_c \leq 7.7 \times 10^{-6}$ were still significantly lower than at $N_c \geq 7.7 \times 10^{-5}$, the CDC suggests that the best suited N_c for hydrogen storage for this micromodel was between $N_c = 7.7 \times 10^{-6}$ -7.7 $\times 10^{-5}$. The flattening of the CDC after $N_c = 7.7 \times 10^{-5}$, indicates a S_{wi} of 33% and 39% for 1 bar and 30 bar, respectively. The immobile water is due to the water-wet nature of the micromodel: the pore network prefers the presence of water and thus hydrogen is not able to displace all of the resident water during drainage. The main reduction in S_w occurred between $N_c = 7.7 \times 10^{-5}$ and $N_c = 7.7 \times 10^{-6}$, which is over an interval of one order of magnitude and the same as the wetting fluid in Figure 1.4. The steep graph over a narrow N_c also indicates a small pore size distribution, which is expected from a synthetically manufactured micromodel with repeated pores and pore channels.

---

[6] S_g were obtained before changing the field of view for imbibition.
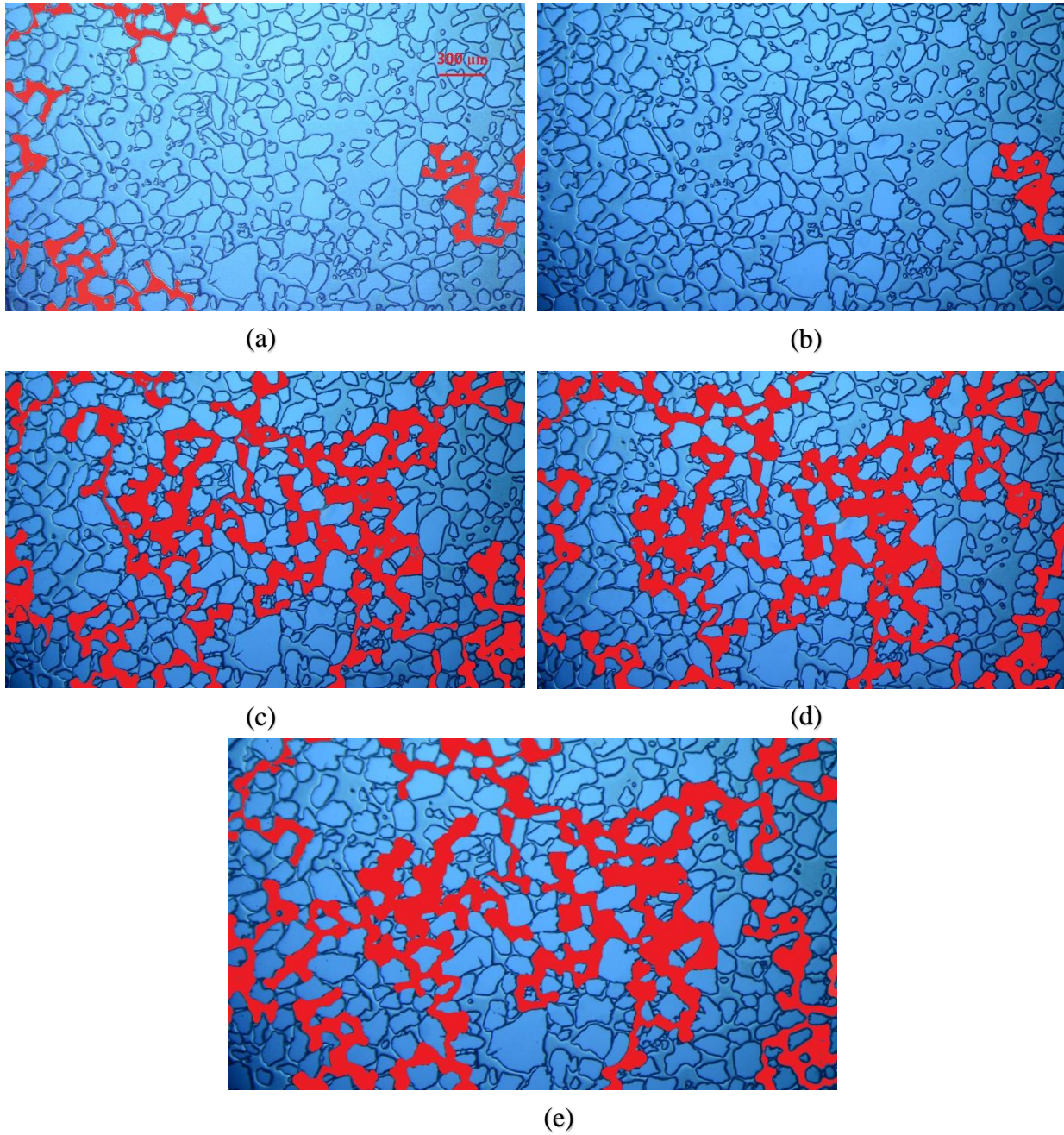
Figure 3.3. Fluid saturation after 100 PV injected hydrogen at 1 bar and different capillary numbers: **a** $N_c = 7.7 \times 10^{-7}$ $S_g = 16\%$. **b** $N_c = 7.7 \times 10^{-6}$ $S_g = 5\%$. **c** $N_c = 7.7 \times 10^{-5}$ $S_g = 65\%$. **d** $N_c = 1.9 \times 10^{-4}$ $S_g = 68\%$. **e** $N_c = 3.8 \times 10^{-4}$ $S_g = 67\%$.

Experiments showed no change in hydrogen saturation between gas breakthrough and an additional 100 PV hydrogen injected. One exception, where it seemed the initial hydrogen was swept away and replenished by new hydrogen suggesting that there most likely was residual

water left in the gas pump tubing from an earlier experiment. The residual water displaced the initial hydrogen in the micromodel, before itself being displaced by additional hydrogen. This specific experiment was thus repeated. A stable gas saturation after breakthrough means there was a stable displacement of the native fluid by the gas and that further injection resulted in hydrogen taking the already established path and water being bypassed.

For low N_c exp. A1 and A2, hydrogen gas did not break through to the large mid-area seen in Figures 3.3a and 3.3b. That area includes some of the largest pores in that field of view (see Figure 3.4). According to equation 1.6, these larger pores should be invaded first and relatively easily, even by low $N_c = 7.7 \times 10^{-7}$ and $N_c = 7.7 \times 10^{-6}$, respectively. When studying Figure 6a closely, it appears that although there is an area with large pores, it is the path leading to these pores causing the obstruction. The hydrogen coming from the upper right tries to reach the larger pores with the lowest capillary pressure, but is prevented by the high capillary entry pressure of the narrow pore throats surrounding the area.
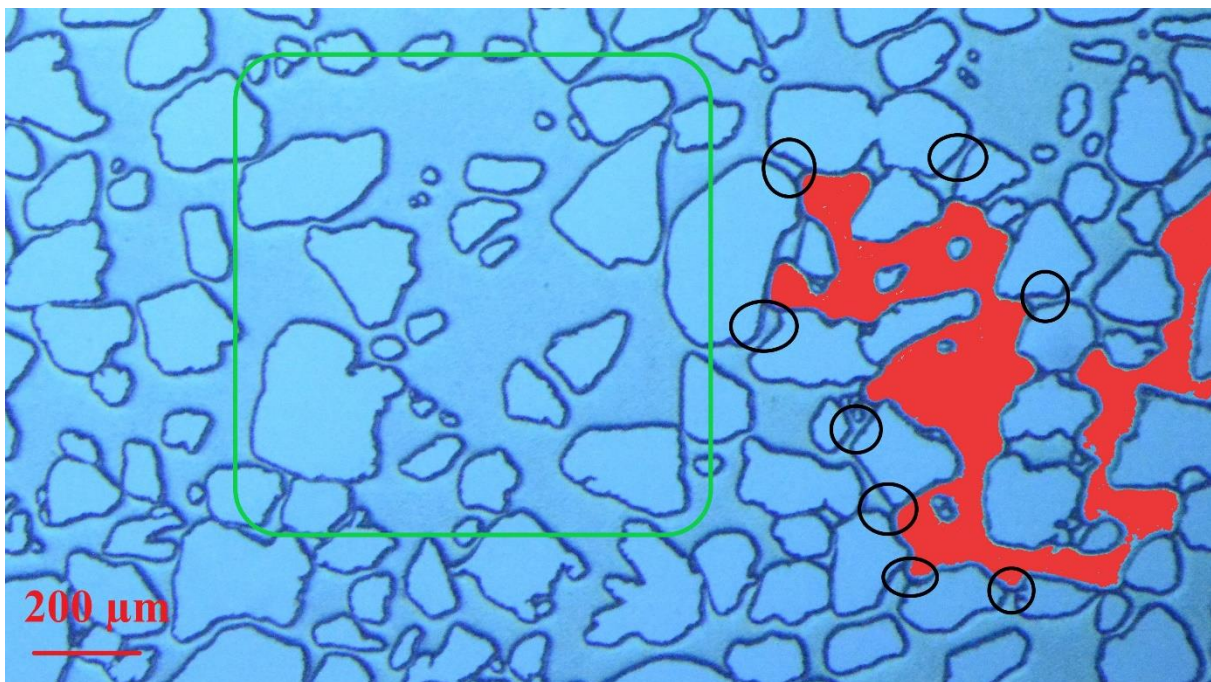
Figure 3.4. Close-up of Figure 3.3a. Hydrogen is prevented by the high-pressure narrow pore throats (black circles) to reach the large unswept area (green rectangle). $N_c = 7.7 \times 10^{-7}$

This phenomenon is most noticeable during drainage immediately after gas breakthrough: the video recording of 3.3a shows that hydrogen tries to squeeze through the narrow pore throats but is pushed back by the capillary entry pressure. This back-and-forth movement happened

multiple times in one second over a period of 20-50 seconds until equilibrium between the viscous and capillary forces was established. As the viscous forces were increased through a higher Q (see equation 1.4 and equation 1.5), hydrogen was able to penetrate these and similar pore throats, and S_g was increased significantly (see Figure 3.3c to 3.3e). However, some stochasticity can also be seen at med N_c: the red area in Figure 3.4 was seen to be invaded by hydrogen in Figure 3.3a, 3.3b, 3.3e, and partially in 3.3c, but not in Figure 3.3d. Meaning, because this area was invaded by the lowest N_c (Figure 3.3a), it has to contain pores with the lowest capillary entry pressures (by definition of equation 1.3), but was not invaded by the second-highest N_c in Figure 3.3d.

3.3 Distilled water imbibition

This chapter discusses results that were obtained during and after water imbibition. A particular focus is on the trapping, dissolution kinetics, and solubility properties of hydrogen under different capillary numbers and pressure regimes. For this study, imbibition was divided into two periods, where period I lasts from the start of water imbibition until local dissolution started, and period II from the start of local dissolution until all hydrogen was dissolved.

The field of view chosen for drainage and imbibition experiments was located in the upper-right corner of the micromodel. The water inlet was located on the opposite side: the lower-left corner (see Figure 2.2). During period I, the waterfront was moving from the inlet (lower-left) to the outlet (upper-right). Behind the waterfront, only water was flowing, while in front of it, both water and hydrogen were flowing. This was observed in every experiment as hydrogen was being swept out and replenished by additional hydrogen at least one or several times. Specifically, this means that for the field of view, during period I dissolution only occurred through diffusion, and dissolution by advection started once the waterfront had reached the field of view, i.e. as the hydrogen was contacted by water. Thus, the reduction in hydrogen saturation from S_g to S_{gr} (see Table 3.4) occurred through a combination of sweep out and diffusion, and reduction from S_{gr} to $S_g = 0$ was through dissolution by advection and diffusion. As section 1.1.3 suggested, dissolution by diffusion during periods I and II were non-existent except for

experiments at $N_c = 7.7 \times 10^{-7}$. During exp. B1, diffusion reduced the hydrogen saturation from $S_g = 21\%$ to $S_g = 20\%$ before the waterfront reached the hydrogen. Similar reductions of 1% in S_g were seen in exp. A1, A6, and B6. These experiments all had imbibition times of around 10 hours (600 min.) and were therefore long enough to be affected by diffusion. As imbibition times were reduced by one order of magnitude for exp. B2, A2, A7, and B7, the resulting S_g reduction may have been in the same order of magnitude (i.e.: reduction from 1% to 0.1%). Because of the relatively small reduction and uncertainty in hydrogen saturation calculation from using Paint 3-D and ImageJ, the effect of N_c and pressure on dissolution by diffusion was not possible to be determined for this study.

Table 3.2. Dissolution and solubility results obtained during imbibition periods I and II.

| Exp. # | N_c | Imbibition time [min] | Dissolution time [min] | Q_d [ng/sec] | $C/C_e \times 10^2$ |
	± 0.3	± 0.2	± 0.2		
A1	7.7×10^{-7}	604.0	144.0	0.005	12.1
A2	7.7×10^{-6}	65.7	33.3	0.03	6.2
A3	7.7×10^{-5}	7.1	6.5	0.7	15.8
A4	1.9×10^{-4}	3.4	1.9	1.7	15.2
A5	3.8×10^{-4}	2.5	0.8	4.0	17.7
B1	7.8×10^{-7}	621.1	56.2	0.7	14.6
B2	7.8×10^{-6}	61.6	16.1	1.6	11.8
B3	7.7×10^{-5}	6.5	4.25	17.8	13.3
B4	1.9×10^{-4}	3.1	1.2	69.4	20.8
B5	3.9×10^{-4}	1.7	0.7	107.8	16.1
A6	7.7×10^{-7}	626.1	67.1	/	/
A7	7.7×10^{-6}	60.5	26.0	/	/
B6	7.8×10^{-7}	636.4	43.3	/	/
B7	7.8×10^{-6}	57.3	13.1	/	/

3.3.1 Trapping mechanisms

At the end of period I imbibition, after the hydrogen had been swept out, the residual hydrogen was observed to be trapped by I1 and I2 snap-off and reduced until S_{gr} (see Table 3.4). The quantity and size of the reduced hydrogen saturation varied with capillary number: at high N_c, the residual hydrogen was divided into many smaller clusters resulting in a lower total S_{gr} (see Figure 3.5b). At lower N_c, the hydrogen phase was trapped into a few continuous clusters over the whole field of view (see Figure 3.5a), resulting in a higher total S_{gr}.
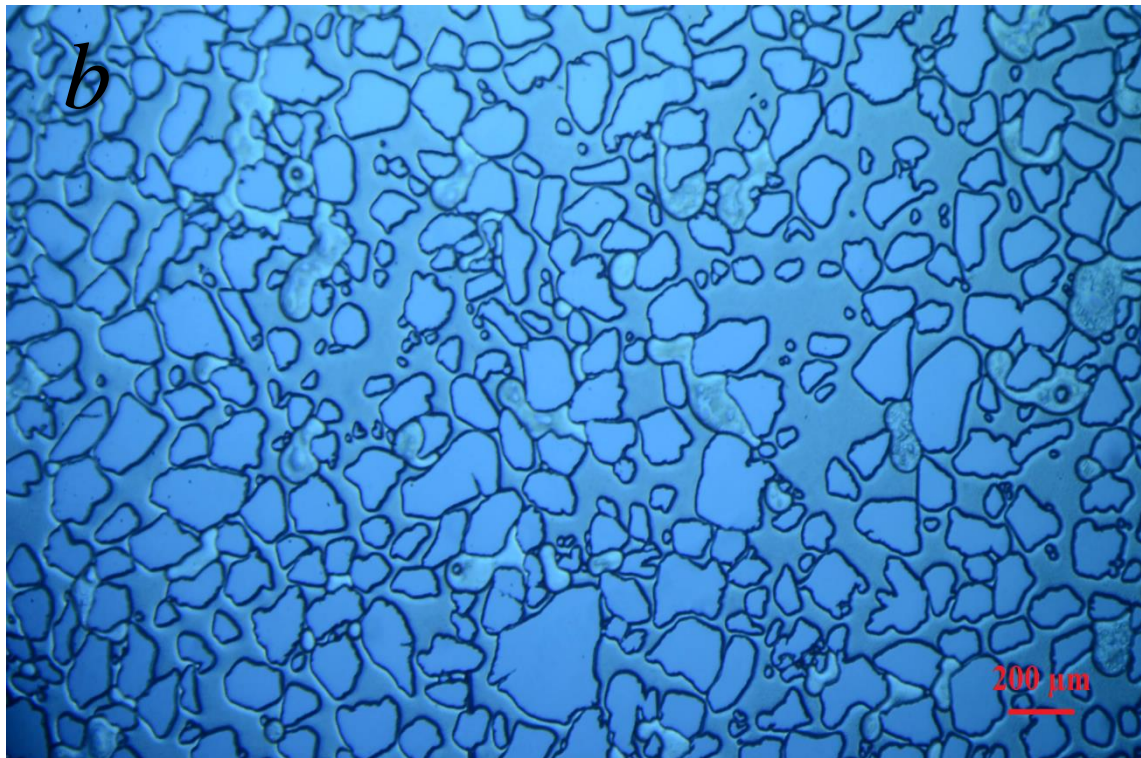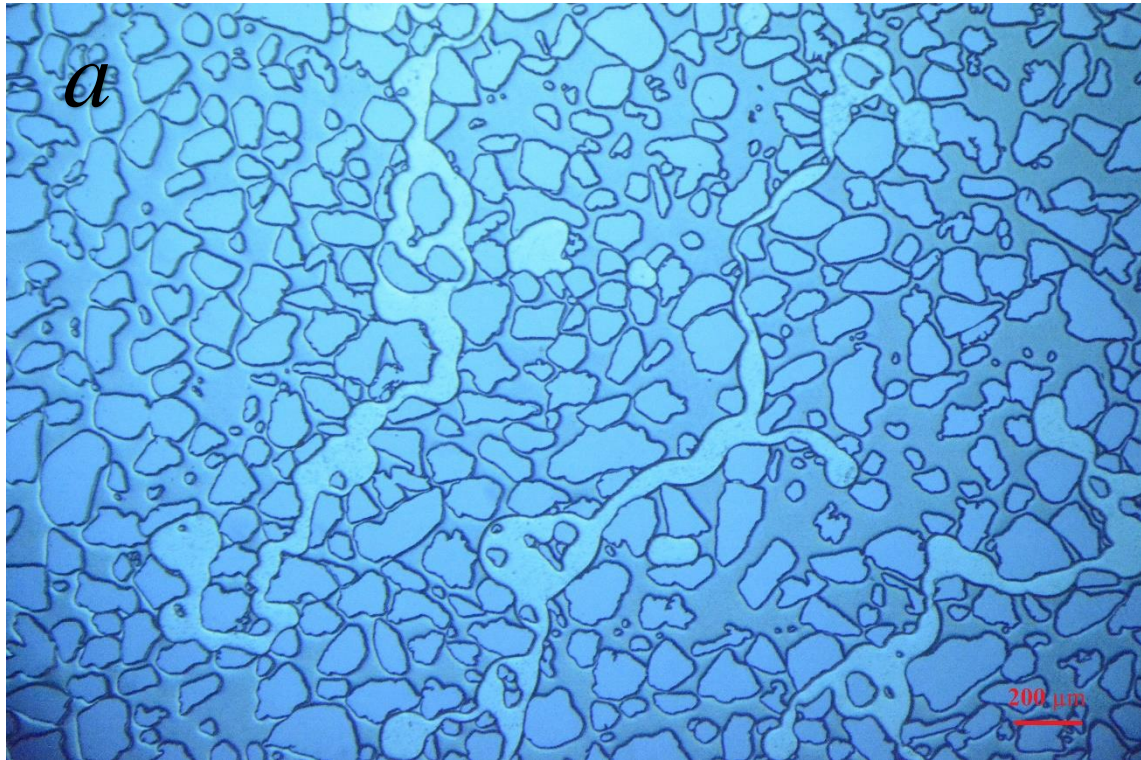
Figure 3.5. The qualitative difference in S_{gr} at high versus low N_c. **a** *Large continuos hydrogen clusters stretched across the field of view. $N_c = 7.7 \times 10^{-7}$.* **b** *Small hydrogen bubbles scattered over the field of view. $N_c = 3.8 \times 10^{-4}$.*

Snap-off was not quantified, but I2 snap-off was dominant throughout every experiment. This can be linked to the tortuosity of the micromodel and long hydrogen clusters that stretched over multiple pores of different sizes and shapes. Due to the tortuosity, large clusters were often forced over the tip of grains that cut hydrogen clusters into two, of which one or both then became trapped and bypassed (see Figure 3.6). The micromodel did not contain a lot of long and straight pore channels, thus the few instances where I1 snap-off occurred, was at low N_c when hydrogen clusters were stretched out and the gas meniscus was located away from the pore walls until it collapsed (see Figure I1 snap-off).
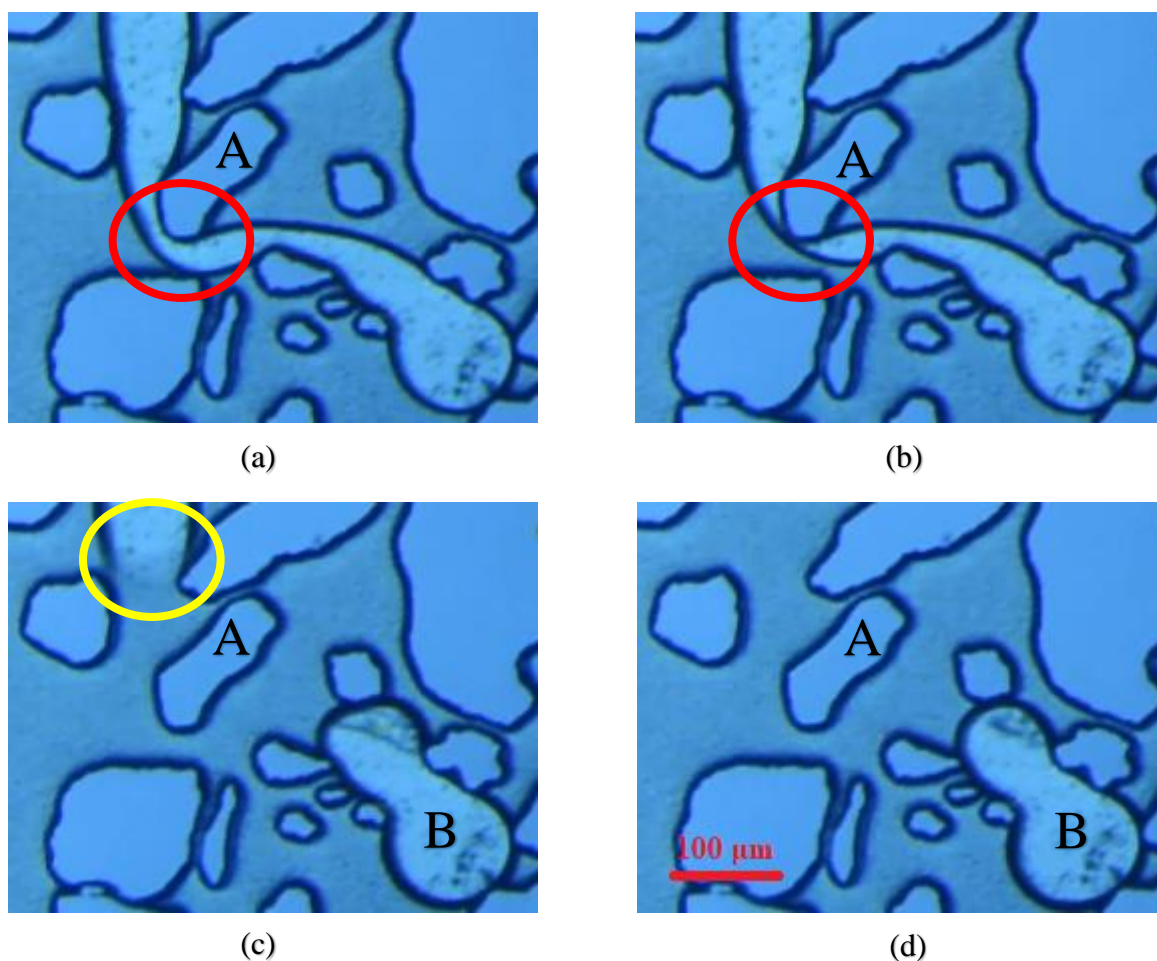
*Figure 3.6. I2 snap-off. The continuous gas phase is being forced into two adjacent pores and collapses once the meniscus reaches the southern tip of grain **A**. Image **c** was taken immediately after the collapse, and thus the upper bubble has not managed to renew its meniscus as it is still receding upwards (yellow circle). Leftover bubble **B** is now discontinuous, bypassed by imbibition, and prone to dissolution. $N_c = 7.7 \times 10^{-6}$ from **a** 0 s, **b** 6.0 s, **c** 7.0 s, **d** 7.1 s.*
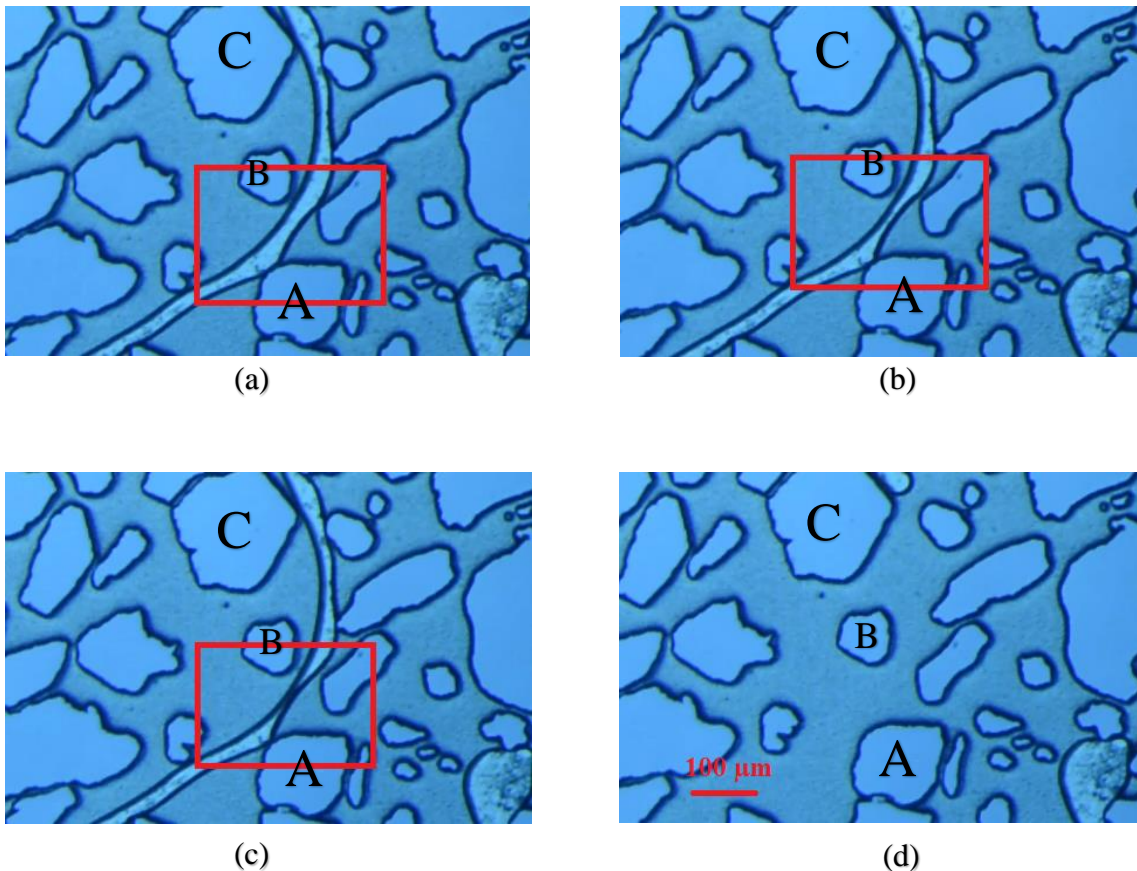
*Figure 3.7. I1 snap-off. The meniscus is stretched thinner until collapse, thus dividing the cluster in two. The roughness of grain **A** acts as an anchor point for the continuous hydrogen phase. At higher N_c, grains **B** and **C** would likely have caused an I2 snap-off instead. $N_c = 7.8 \times 10^{-7}$ from **a** 0.0 s, **b** 7.0 s **c** 14.9 s **d** 16.2 s.*

Figure 3.7c shows that the roughness of grain A acts as an anchor point for the continuous hydrogen phase, thus making an I1 snap-off possible as the meniscus is stretched thinner and away from the pore wall. The stretching occurred due to sweep out and/or dissolution of the cluster at both ends. At higher N_c, the roughness of grain A most likely would not have been enough to keep the hydrogen attached to it and there would have been a high probability that instead of I1, an I2 snap-off would have occurred at the tip of either grain B or C. This observation might be an indication of why there were no visible I1 snap-offs at higher N_c.

3.3.2 Hydrogen imbibition- and dissolution time

This chapter focuses on analyzing hydrogen dissolution and depletion using recorded videos and interval pictures. The main focus was how the imbibition- and dissolution times change in regards to capillary number and pore pressure.

For exp. A3 a hydrogen saturation of 65% was obtained after drainage (see Table 3.1). At a rate of 10 mL/h ($N_c = 7.7 \times 10^{-5}$), it took approximately 7 minutes to reach the reduced hydrogen saturation of 32% (see Table 3.2). The residual 32% hydrogen was then dissolved in 6 minutes. As mentioned in chapter 3.3, due to the low effect of diffusion at $N_c > 7.7 \times 10^{-7}$, the reduction from $S_g = 65\%$ to $S_{gr} = 32\%$ occurred primarily from sweep out, i.e. hydrogen was displaced by the injected water. The dissolution of the remaining 32% hydrogen was through advection by the water phase. Because of the water-wet nature of the micromodel, water swept the smallest pores with the highest capillary pressure first, and bypassed the residual hydrogen (S_{gr}) located in the larger pores. Thus, the pore-scale displacement of hydrogen during imbibition is the opposite of water during drainage, where hydrogen displaced water in the largest pores first.

Imbibition time was reduced by a large margin at different N_c but remained roughly the same for different pressure regimes. For exp. A1, A2, A3, B1, B2, and B3, N_c was increased by one order of magnitude, while the imbibition time was decreased by approximately the same order of magnitude (A1: 604 min; A2: 66min; A3 7 min and B1: 621 min; B2 62 min; B3 6.5 min). Additionally, imbibition times also seem to correlate to the amount of hydrogen injected during drainage. Meaning, 100 PV water was injected before dissolution started. In equilibrium, injecting 100 PV (1 mL) water for $Q = 0.1$ mL/h, 1.0 mL/h, and 10 mL/h would thus have taken 600, 60, and 6 minutes, respectively. These equilibrium durations correspond to a deviation of A1: $\frac{604\ min}{600\ min} = 1\%$, A2: $\frac{66\ min}{60\ min} = 9\%$, A3: $\frac{7\ min}{6\ min} = 14\%$, B1: $\frac{621\ min}{600\ min} = 4\%$, B2: $\frac{62\ min}{60\ min} = 3\%$, and B3: $\frac{6.5\ min}{6\ min} = 8\%$. For the remaining experiments at high N_c, imbibition time was reduced but not in the same order of magnitude as N_c was increased, nor equal to the time it took to inject 100 PV of water. In equilibrium, dissolution time of 3.4 minutes for exp. A4, and 2.5 minutes for exp. A5, would have been 2.4 and 1.2 minutes, respectively. The deviation from equilibrium durations for these two experiments is thus A4: $\frac{3.4\ min}{2.4\ min} = 42\%$ and A5: $\frac{2.5\ min}{1.2\ min} = 108\%$. This indicates that there might be a less stable displacement at higher N_c and conditions that are more difficult to quantify due to the rapid nature of the experiments.

Contrary to imbibition time, Table 3.2 shows that dissolution time strongly depended on pressure and N_c: at 1 bar, the highest dissolution time was 144 minutes (exp. A1), and the lowest was 0.8 minutes (exp. A5). At 30 bar, the highest dissolution time was 56.2 minutes (exp. B1), and 0.7 minutes (exp. B5). Depletion rate was inversely proportional to dissolution time, meaning experiments with a short dissolution time had a high Q_d. For 1 bar, Q_d ranged from 0.005 nanograms per second (ng/sec) to 4.0 ng/sec for exp. A1 and A5, respectively. As the pressure was increased to 30 bar, Q_d ranged from 0.7 ng/sec (exp. B1) to 107.8 ng/sec (exp. B5). The results show the effect of pressure and N_c on dissolution for the total hydrogen saturation in the micromodel. However, the quantification obtained in Table 3.1 only shows the beginning and end of the processes, and an in-depth look at Q_d will be further discussed in the next sections.

3.3.3 Pore-scale Hydrogen-bubble dissolution and depletion rates

For each experiment, one or more hydrogen bubbles and/or clusters were analyzed to better understand which pore-scale phenomena occur during dissolution. As mentioned in section 3.2.1, the hydrogen saturation was limited for experiments at $N_c \leq 7.7 \times 10^{-6}$ (see Figure 3.3a and 3.3b), and to be able to analyze hydrogen bubbles at all N_c, these had to be repeated with a slightly different field of view for exp. A6, A7, B6, and B7. Because this section investigates single hydrogen bubbles and not general fluid saturations, a change in the field of view would not affect the outcome. However, to obtain as identical conditions as possible, the new field of view was chosen in the same upper-right area of the micromodel as the previous experiments.

3.3.3.1 Hetero- and Homogenous dissolution

When analyzing videos of individual hydrogen bubbles, different types of dissolutions were observed. During some experiments, the bubbles dissolved *homogeneously*, meaning dissolution occurred from all sides of the bubble simultaneously. In other examples, dissolution occurred at only one part of the bubble in a *heterogeneous* dissolution. Figure 3.8 shows the dissolution of a smaller bubble that was trapped during period I imbibition. In the first two

images, it appears to be a heterogeneous dissolution along the roughness of the pore wall, but Figure 3.8c shows that dissolution was homogenous and pore walls were a natural obstruction, and not acting as a trap. A heterogeneous dissolution can be observed in Figure 3.9. The hydrogen gas bubble is trapped by the roughness of the pore wall and dissolved by the water flow coming from the bottom left corner.

(a)

(b)

(c)

(d)
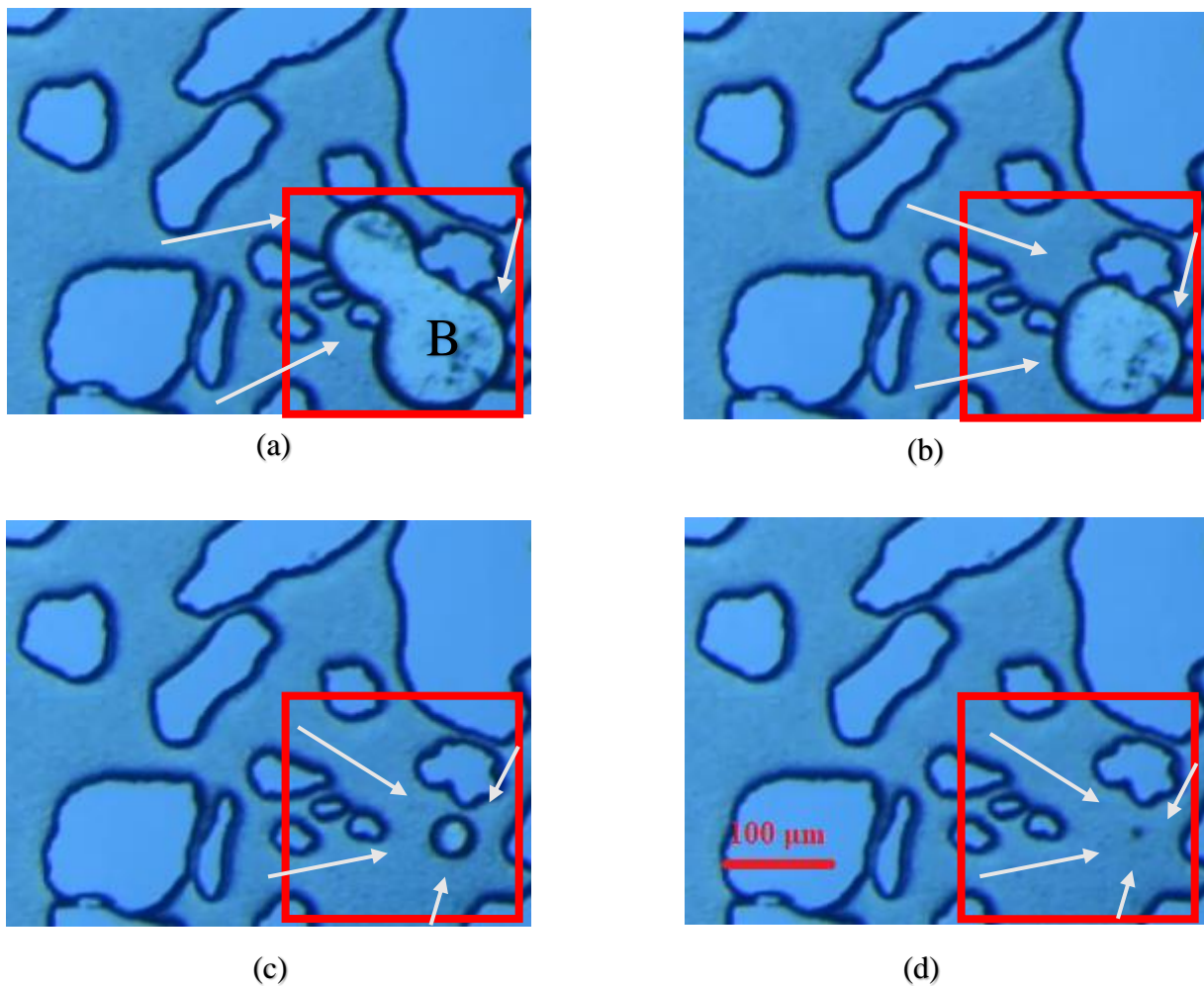
Figure 3.8. Bubble B from figure undergoing a homogenous dissolution at $N_c = 7.7 \times 10^{-6}$. Water flow direction is indicated by the white arrows. **a** *0 s,* **b** *33 s,* **c** *104 s,* **d** *122 s.*
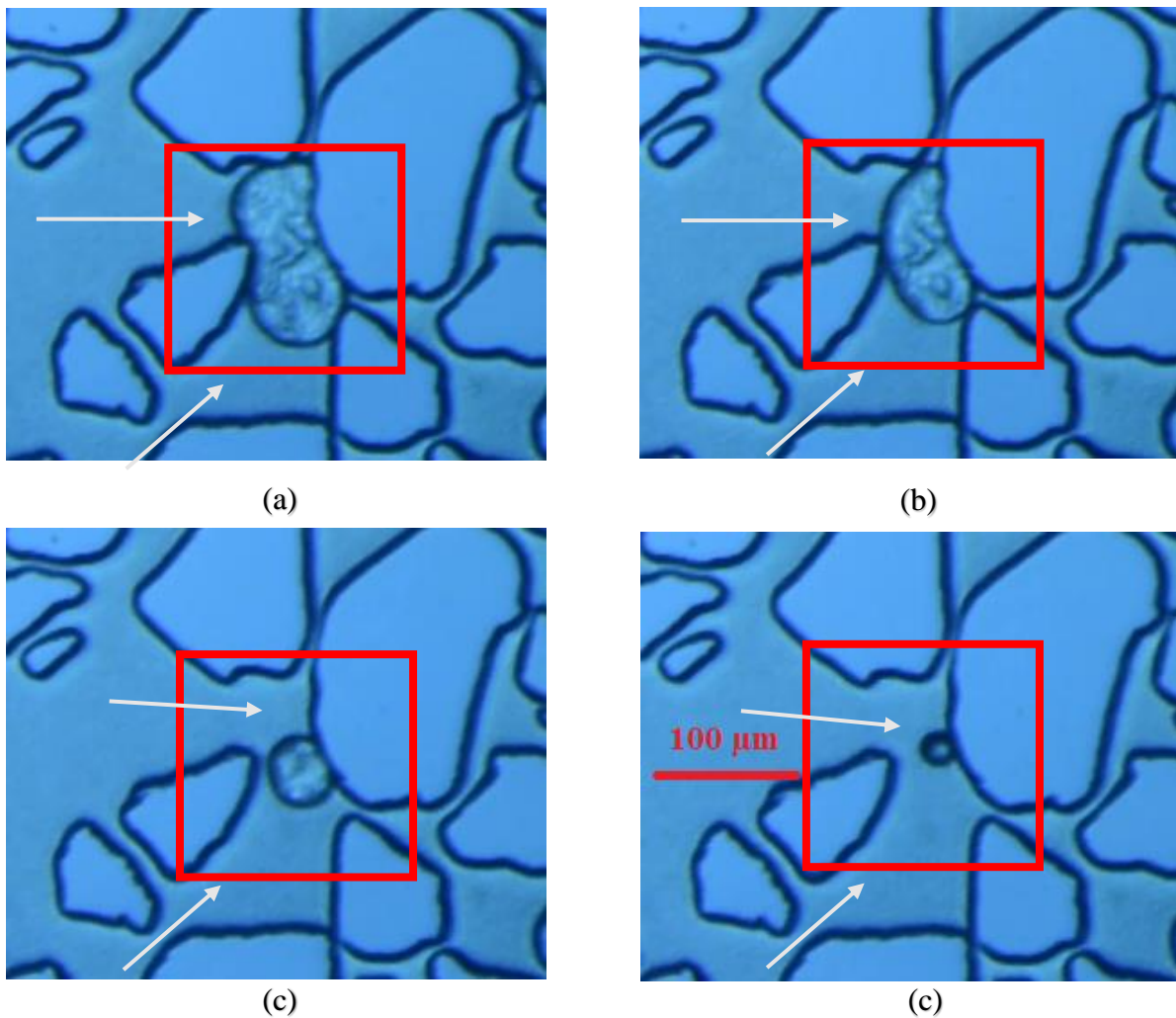
Figure 3.9. Heterogeneous dissolution along the pore wall at $N_c = 3.8 \times 10^{-4}$*. Water flow direction is indicated by the white arrows.* **a** *0 s,* **b** *3 s,* **c** *7 s,* **d** *10 s.*

Due to the high number of bubbles after drainage, hetero- vs homogenous dissolution was not specifically quantified during this study, but experiments showed that heterogeneous dissolution was dominant throughout. This domination can be attributed to the injected water coming from one side of the micromodel. Especially at higher N_c, the water flow coming from the lower left was forcing the bubbles to adhere onto the roughness of the pore wall on the upper right side parallel to the water flow (see Figure 3.10). Afterward, heterogeneous dissolution seemed to exclusively start from the left side of the bubbles during the early- and mid-period II imbibition.

The few experiments where homogenous dissolution was observed, were at low N_c and during the very late period II imbibition. In these cases, homogenous dissolution might be accredited

to what Chang et al. (2016) described as *transverse water flow*. During this stage, water had already been injected over a longer period, which resulted in the micromodel becoming "oversaturated" with water, and water flow direction changing from coming only from one side of the micromodel (i.e.: from where the water inlet was located), to multiple directions from every part of the model. The change from single- to multi-directional flow allowed hydrogen bubbles to be homogenously dissolved at the total available interface.
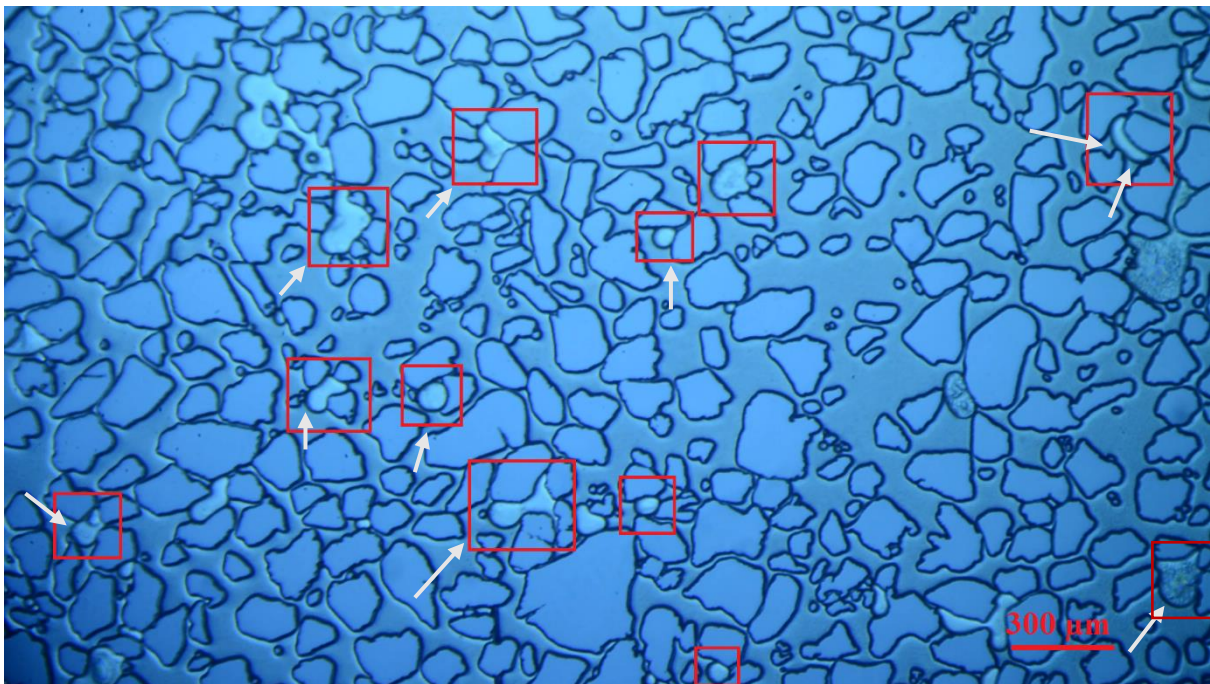
Figure 3.10. Right before dissolution starts (i.e.: transition between imbibition period I and II), bubbles are forced into corners or roughness of pore walls along the water flow direction indicated by the white arrows. $N_c = 3.8 \times 10^{-4}$.

3.3.3.2 Advection

For the chosen N_c, the main contributor to dissolution was advection, or how much of the bulk fluid (water) was in motion at a given time. As seen in Figure 3.11a, advection is strongly dependent on N_c. During higher N_c, a larger amount of fresh distilled water was constantly being replenished at the water-hydrogen interface, thus increasing dissolution. A hydrogen bubble with an area of 21.000 μm^2 took 22 seconds to dissolve at high N_c, while it took 93 seconds to completely dissolve the same area at low N_c. Figure 3.11b shows the same bubbles

plotted against pore volume in a reverse trend: Low N_c uses 1/10 the amount of water volume to completely dissolve an equal area, compared to medium and high N_c. The high effect of low versus high N_c dissolution has also been observed during experiments with CO_2: "The total PV needed for complete dissolution represents the effectiveness of dissolution per unit volume of water. The effectiveness inversely depends on the injection rate […]." (Chang et al., 2016). Indicating that low injection rates, or N_c, used less water volume to dissolve CO_2.

This *effectiveness* is not explained specifically by Chang et al. at that time, but may be related to *residence time* discussed by some of the same authors in 2019 (Chang, Zhou, Kneafsey, Oostrom, & Ju, 2019). Longer residence time at low N_c allows for a longer contact between hydrogen and mobile water which will increase dissolution and mass transfer (per injected volume of water). In addition, because of the water-wet silica used in this experimental study, water flow may occur as a thin film along the surface of the pore network. The swelling of the water film has been observed to increase dissolution around the pores. An increase in N_c will thus shorten the swelling time and reduce the effectiveness of dissolution.
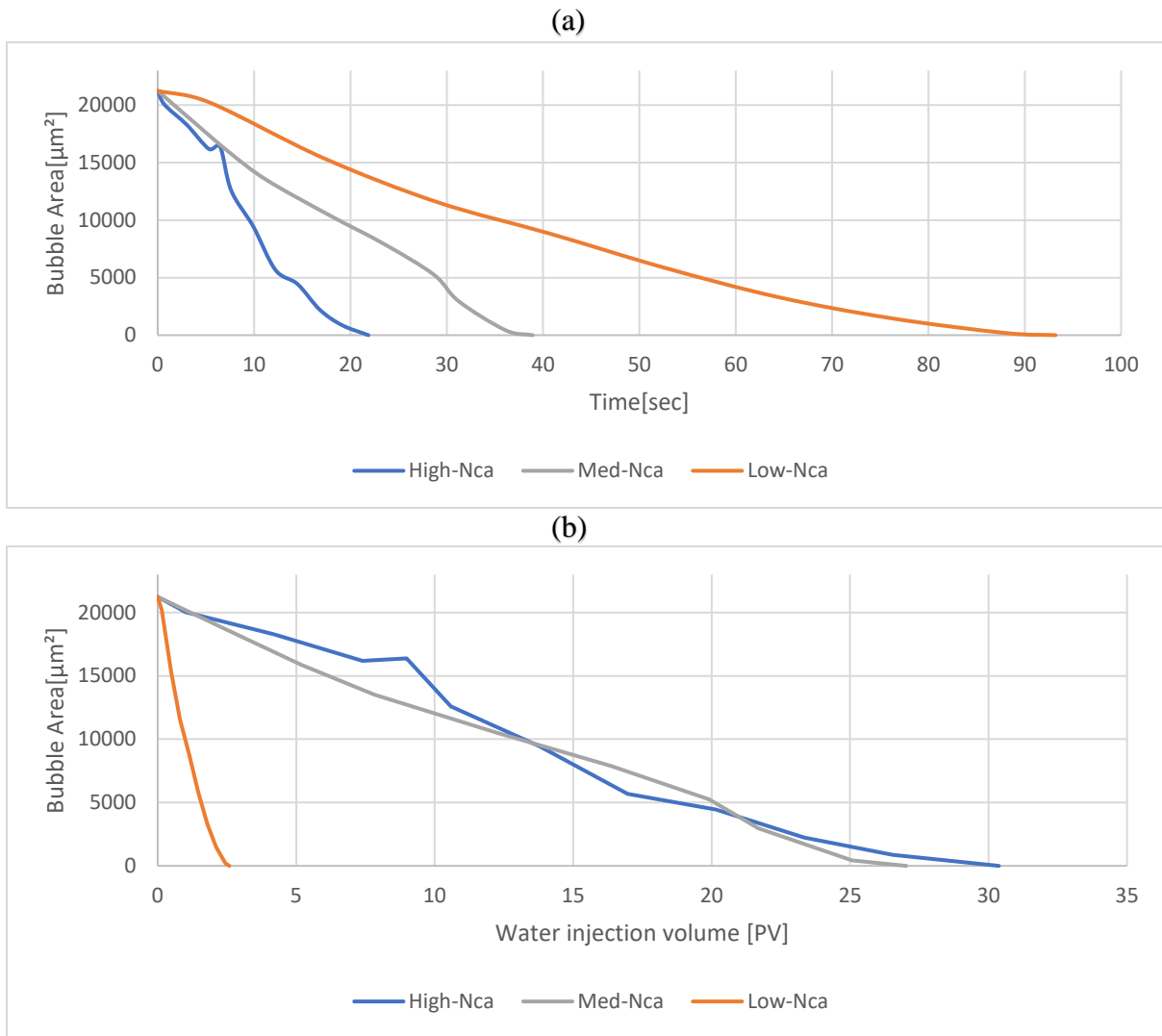
Figure 3.11. The depletion of equally sized hydrogen bubbles during water imbibition with high-, med-, and low capillary numbers. **a** *Per second.* **b** *Per pore volume.*

3.3.3.3 Water-Hydrogen interface

When studying videos and interval pictures of individual hydrogen bubbles alongside their respective depletion rate graphs, it became apparent that the water-hydrogen interface influenced the pore-scale dissolution processes of hydrogen. The larger the hydrogen bubble, the larger the interface between the injected water and resident hydrogen. Once dissolution had been initiated, Q_d declined as the interface decreased with the bubble's size. Because spheres have the lowest surface area to volume, a spherical hydrogen bubble had a lower Q_d than an equally sized cluster with a random shape. This statement, however, only holds under optimal conditions, and it is important to note that other factors may influence Q_d as well. As discussed in 3.2.2.1, a hydrogen bubble will either form on the roughness on the pore wall on one or

several specific spots (see Figure 3.8), or away from the pore wall as a free bubble (see Figure 3.7). In both cases most of the water-hydrogen interface changes due to the shrinkage of the bubble itself during dissolution, thus the Q_d is gradually decreasing in a "stable" manner (see Figure 3.12b). Hydrogen clusters, however, will adhere exclusively to the pore walls, and as the cluster is dissolving, it will change form and interface multiple times which will result in a Q_d with a seemingly random pattern of high oscillations (see Figure 3.12c). Although, when studying hydrogen images alongside Q_d, these patterns may be explained to a certain degree: in Figure 3.12a, between 0-7 seconds, the cluster has a fair amount of water-hydrogen interface, but most of the energy of the injected water phase is used to sweep hydrogen and invade a pore (indicated by the yellow star) instead of dissolving the hydrogen, and thus the corresponding Q_d during that period is below one picogram per second (pg/sec). After 7 seconds, the cluster had been stabilized at the pore walls, and Q_d rises to almost three pg/sec and then declines as the cluster shrinks in size. At 62 seconds, the entire southern part of the cluster had been dissolved, and only the previously invaded pore contains hydrogen. This pore has only two very small pore throats of approximately 2-4 µm, thus the interface is equally small and Q_d reaches 0 for a short period. Once a small amount of the trapped hydrogen had been able to dissolve, the bubble moved away from the pore wall and a larger interface was available again (as seen at 74 seconds), and Q_d reaches 1 pg/sec again.

Experiments in Figure 3.12a and 3.12c had the same N_c but were conducted at 1 and 30 bar, respectively. Thus, their individual Q_d varies by more than one order of magnitude. This shows that the water-hydrogen interface dictates the oscillation of Q_d within a range that is controlled by the pressure (i.e.: ranging from 0 to 4 pg/sec for a, and 0 to 90 pg/sec for c). At high N_c, it was at times difficult to differentiate between sweep out and dissolution during the start of period II imbibition. This could be seen by the cluster in Figure 3.12a, where there was a combination of dissolution and sweep out that gave a distorted Q_d between 0 and 7 seconds. As mentioned in section 3.3.3.1, dissolution was dominantly initiated from the lower left where the water inlet was located, thus homogenous dissolution and a stable declining Q_d as seen in Figure 3.12b was rare and only observed at low-med N_c.
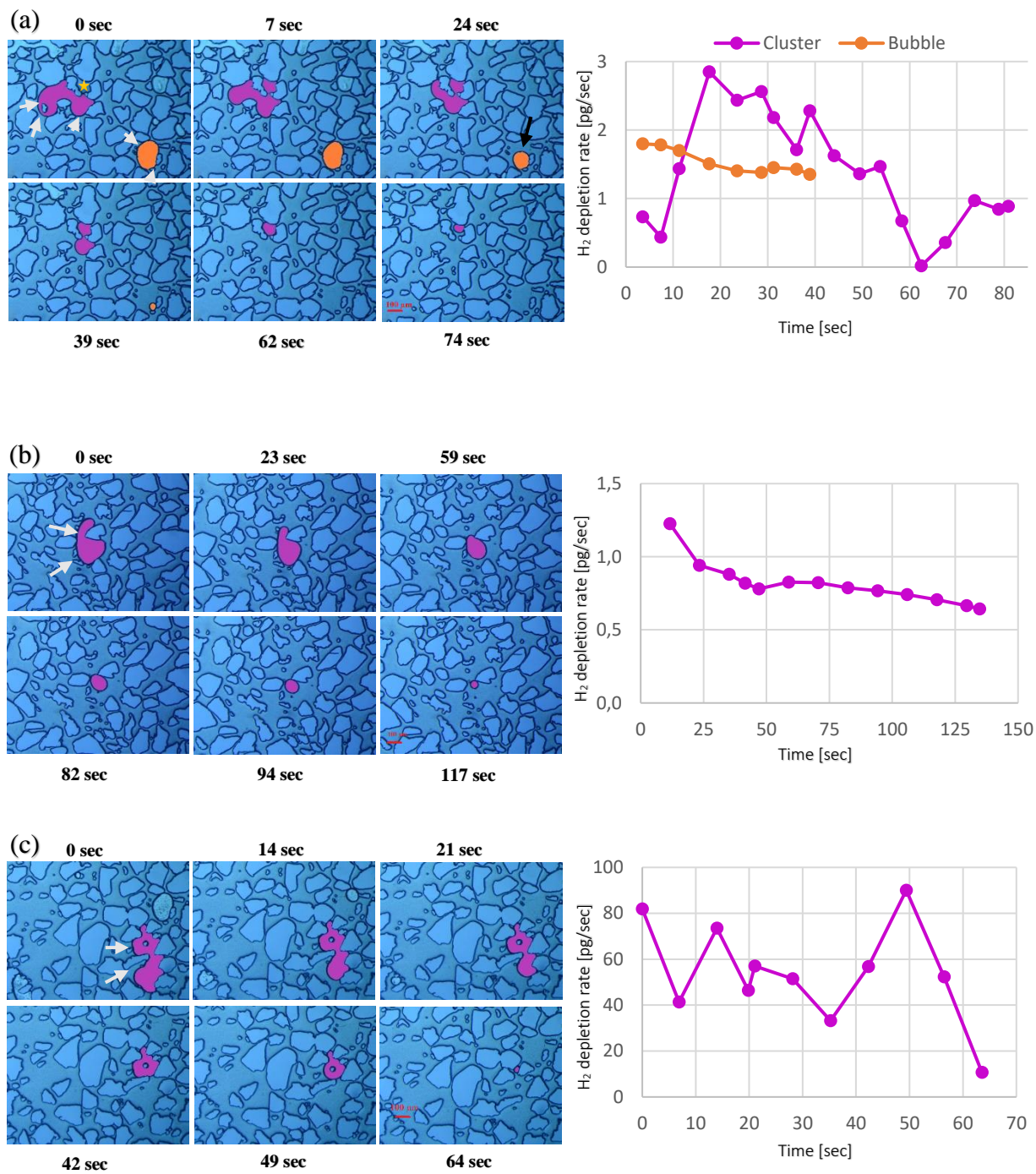
*Figure 3.12. Visualization of shrinking hydrogen clusters and bubbles and their respective depletion rates. White arrows indicate the flow direction. **a** Stable bubble depletion (orange) and changing cluster (purple). The black arrow indicates a newly created water-flow path. $N_c = 1.9 \times 10^{-4}$ **b** Cluster-bubble hybrid with a mostly stable depletion rate. $N_c = 7.7 \times 10^{-6}$ **c** Cluster with constantly changing interface and highly oscillating depletion rate. $N_c = 1.9 \times 10^{-4}$*

Another factor that influences both macro and pore-scale dissolution of hydrogen is the creation of new water-flow paths. This is described in detail by Chang et al. (2016), where they state that while certain areas with gas are being dissolved, more paths leading to other gas bubbles are becoming available, and thus higher dissolution and depletion rates may occur for the remaining bubbles. Because hydrogen was mostly trapped as clusters at the roughness of pore walls, this phenomenon was not often observed during this experimental study, but an example can be seen in Figure 3.12a at 24 seconds. In this case, a new path created by the change from single- to multi-directional water flow (as described in 3.3.3.1) leads to a homogenous dissolution of the orange-colored hydrogen bubble. Additionally, as new paths arise, more water-hydrogen interface become available, thus, the creation of new water-flow paths is in direct relation with the increased interface discussed in this section and therefore redundant to investigate specifically.

3.3.4   Hydrogen solubility in water

Solubility was calculated by the amount of injected water volume and hydrogen saturation of the micromodel. In addition to the homogeneously distributed fluid saturation throughout the micromodel made in section 3.2, the assumption of a stable waterfront moving inside the micromodel and contacting the resident hydrogen simultaneously was made.

Similar to dissolution, solubility was also affected by increased capillary numbers, but a more important factor was the pressure inside the micromodel (see Figure 3.13). At 1 bar, the average solubility was increased by a factor of 2.5 $\left(\frac{c_{A2}}{c_{A1}}\right)$ when increasing N_c from 7.7×10^{-6} to 7.7×10^{-5}, and only by a further factor of 1.2 $\left(\frac{c_{A5}}{c_{A3}}\right)$ from $N_c = 7.7 \times 10^{-5}$ to $N_c = 3.8 \times 10^{-4}$. As the pressure was increased from 1 to 30 bar for the same N_c[7], solubility increased by a factor of 125 $\left(\frac{c_{B1}}{c_{A1}}\right)$, 57 $\left(\frac{c_{B2}}{c_{A2}}\right)$, 25 $\left(\frac{c_{B3}}{c_{A3}}\right)$, 34 $\left(\frac{c_{B4}}{c_{A4}}\right)$, and 27 $\left(\frac{c_{B5}}{c_{A5}}\right)$ for $N_c = 7.7 \times 10^{-7}$, $N_c = 7.7 \times 10^{-6}$, $N_c = 7.7 \times 10^{-5}$, $N_c = 1.9 \times 10^{-4}$ and $N_c = 3.8 \times 10^{-4}$, respectively. In Chabab et al.'s (2020) study, the solubility of hydrogen in distilled water[8] increases by a factor of 29 for the same pressure range of 1 to 30 bar. Although Chabab et al.'s study was conducted under equilibrium

---

[7] N_c were considered the same, but in reality, due to the minor effect of pressure on viscosity and interfacial tension, N_c for equal Q during exp B1-B5 were slightly higher than for A1-A5 (as seen in Table 3.1).
[8] The study states 0 mol NaCl/kgw, thus assumed to be distilled water.

conditions with a different experimental setup, the dimensionless ratio between the solubility at different pressures is still a valid comparison to this study. The increased factor of 29 under equilibrium conditions is close to the experimental results from $N_c = 7.7 \times 10^{-5}$ (factor of 25), $N_c = 1.9 \times 10^{-4}$ (factor of 34), and $N_c = 3.8 \times 10^{-4}$ (factor of 27) of this study.
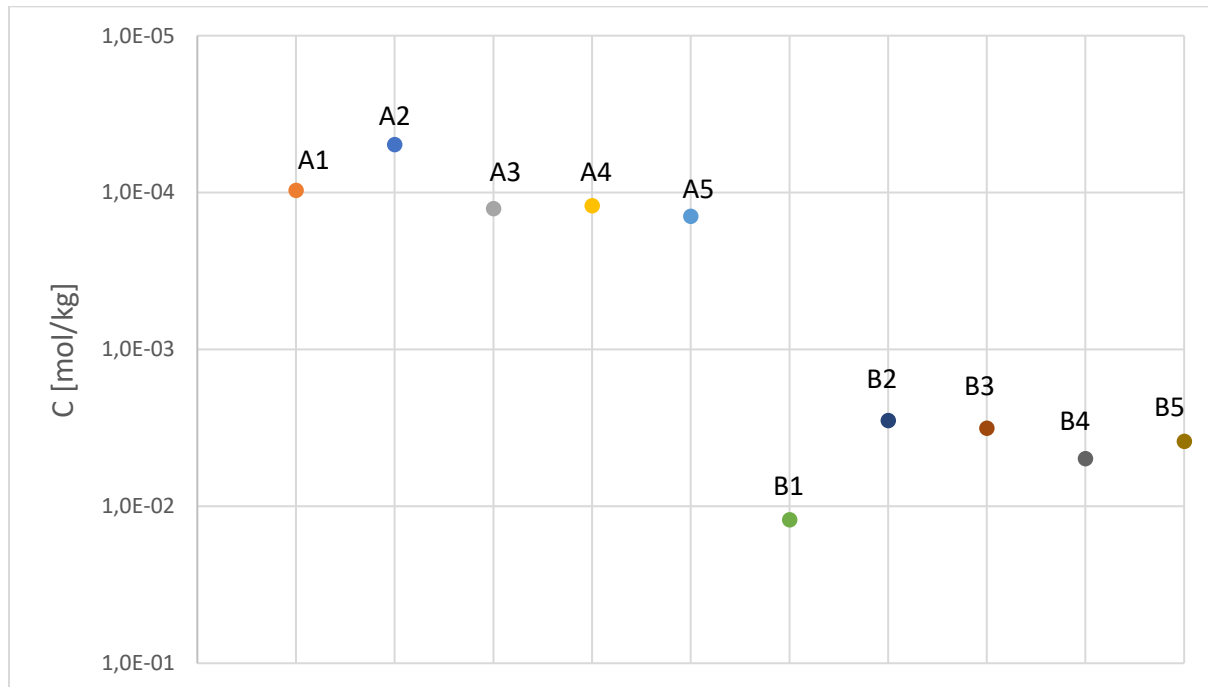
Figure 3.13. Average hydrogen solubility in mol hydrogen per kg water during water imbibition. Experiments A1-A5 and B1-B5 were conducted at 1 bar and 30 bar, respectively. Solubility increased by a factor of 125 (B1/A1), 57 (B2/A2), 25 (B3/A3), 34 (B4/A4), and 27 (B5/A5).

The large factors of 127 and 57 for low N_c indicate high uncertainty for solubility calculations at low S_g. This inaccuracy can further be observed when analyzing the ratio of the calculated solubility to the equilibrium solubility under optimal conditions (C/C_e) (see Table 3.2). Because dissolution is proportional to solubility, and both C/C_e and effectiveness (Figure 3.11b) are a function of the injected water volume, they should follow the same trend, i.e. a lower N_c should result in a higher C/C_e. However, solubility results from these experiments show a reverse trend: higher N_c resulting in higher C/C_e. Because of this inconsistency, the solubility concentration of individual hydrogen bubbles was quantified and analyzed additionally. The hydrogen concentration solubility was measured based on the volume of

hydrogen bubbles contacted by water, and the mass of water injected between a known time interval. The equation used was:

$$C_c = \frac{d \Delta A \rho_{H_2}}{M_{H_2} Q \Delta t \rho_{H_2O}}$$ (3.1)

where C_c is the hydrogen solubility concentration [mol H_2/kg H_2O], ρ_{H_2O} is the density of hydrogen [g/mL], d is the pore depth [30 µm], ΔA is the change in area [µm^2] of the hydrogen bubble over a known time interval Δt [sec], ρ_{H_2} is the density of water [g/mL], and M_{H_2} is the molar mass of hydrogen [2.016 g/mol].

Figure 3.14 shows the range of concentration for one or more clusters and the average concentration over the entire dissolution. The minimum concentration varies from 0.2 for B5 to 6.2 for A6. The maximum concentration varies from 1.7 for B5 to 43.3 for B6. The average concentration ranges from 0.8 for B5 to 26.0 for B6. These results show that lower N_c gives a higher C_c/C_e and therefore better compliance with effectiveness observed during dissolution and Figure 3.11b. When extrapolating the average hydrogen solubility concentration in Figure 3.14, one can assume that equilibrium solubility can be achieved with long resident times at very low N_c. Indicating that, although dissolution through advection is low at typical conditions for groundwater flow ($N_c \approx 4.9 \times 10^{-8}$), effectiveness is high and might reach equilibrium solubility. However, at flow rates typical for water injection during gas production ($10^{-7} < N_c < 10^{-4}$), effectiveness is low but dissolution is high. Hence: for hydrogen storage and withdrawal, N_c that are low enough for reduced dissolution due to advection, but high enough to avoid reaching equilibrium solubility should be considered.
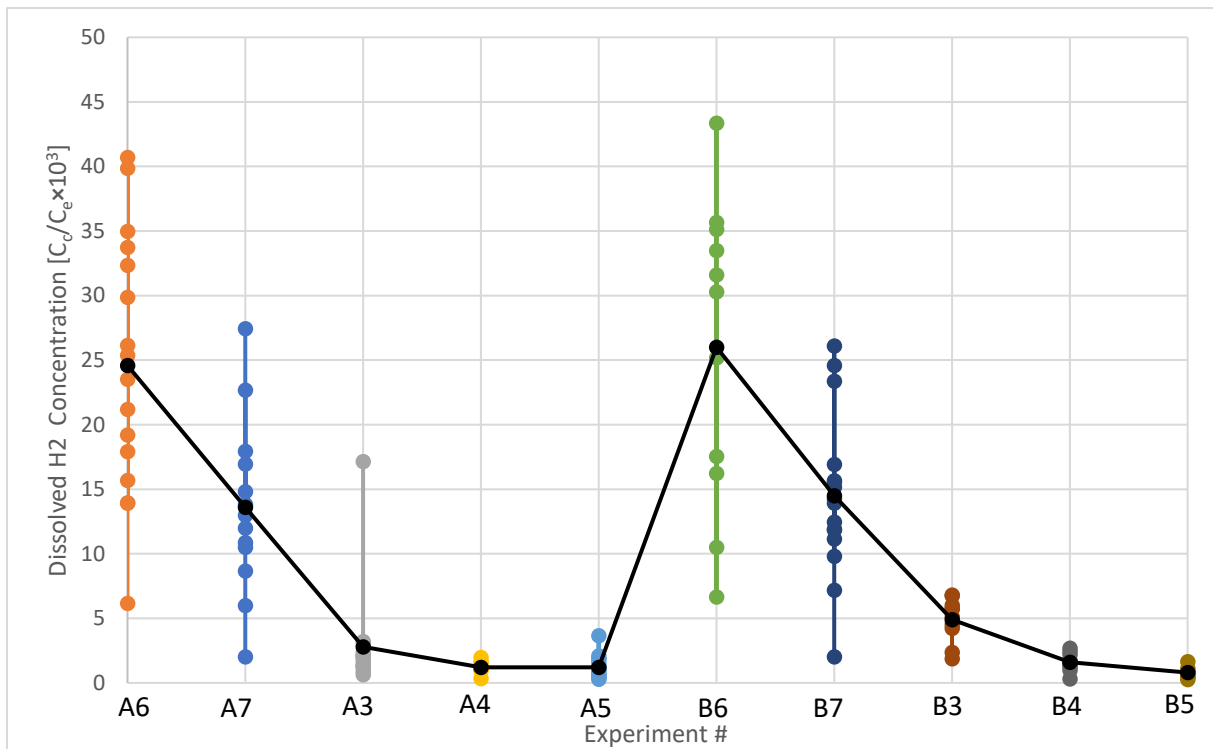
Figure 3.14. Varying hydrogen bubble concentration to equilibrium solubility during experiments A3-A7 and B3-B7. The black line indicates the average for each experiment.

Furthermore, these dissolution and solubility results were achieved with distilled water and are not representative of a real aquifer. Depending on the depth and location, a natural aquifer's salinity can vary between 1 and 38 gram NaCl per liter H_2O (de Montety et al., 2008), which equals 0.02 to 0.7 mol/kgw, respectively. These salinities would correspond to a reduction of 1.4% to 17% in solubility (see Figure 1.7). The reduction indicates that the solubility results obtained during this thesis would be an overestimation when applied to real aquifers and that deeper and saltier reservoirs are preferable to shallower and fresher. However, when transitioning from distilled to saline water conditions, there are more factors than just the effect on dissolution and solubility that have to be considered (e.g.: corrosion and bacteria accumulation).

3.4 Further discussion

Round-trip efficiency is one of the major deciding factors whether underground hydrogen storage is profitable and, like oil and gas extraction, a small variation in recovery can potentially be the difference between a successful or failed operation. In Lord et al.'s (2011) example, which is based on an aquifer in the Yeso Formation, the working gas is estimated to be 7,164 tonnes of hydrogen. A 1% swing in recovery will therefore mean a $360,000 difference (assuming injection of green hydrogen at 5$/kg production cost).

From the experimental results, the reduced gas saturation S_{gr} is hydrogen that was not able to be swept out under period I imbibition and is, therefore, capillary trapped and potentially lost to dissolution. The difference between the saturation after drainage, S_g, and S_{gr} is therefore the percentage of swept or recovered hydrogen (see Table 3.4). Due to a pore volume of only 0.01 mL, an accurate material balance was not possible to conduct. Thus, based on the assumption of homogeneous fluid saturation throughout the micromodel made in section 3.2, the following equation was used to determine the amount of hydrogen recovered:

$$V_r = (S_g - S_{gr})V_P \qquad (3.2)$$

where V_r is the recovered volume of hydrogen [µL] and V_p is the pore volume of the micro model.

The lowest total hydrogen recovery was 0.4 µl (exp. A6), and the highest was 5.3 µl (exp. A5). The lowest percentage recovered was 52% for both exp. A3 and A7, and the highest was 88% for exp. A6. The fact that exp. A6 has the most hydrogen recovered in percent, but the least in the total amount gives again reason to believe saturation calculations at low N_c contain an increased uncertainty for this micromodel and selected field of view. Section 3.3.4 also states that the effectiveness of solubility (and thus also dissolution) increases with decreasing N_c, which should result in more dissolution and lower recovery of hydrogen at low N_c. In exp. A3-A5 and B3-B5 there is a clear trend that follows an increase in both total amount and percentage of recovered hydrogen as N_c increases. The exceptions were 67% and 66% for exp. B3 and B4, respectively; a small deviation that can be explained by uncertainty in hydrogen mapping using Paint 3-D and ImageJ.

Table 3.4. Hydrogen recovery in total volume and percentage during imbibition.

Exp. #	N_c ±0.3	S_g	S_{gr}	Recovery [%] ±2	V_r [µl] ±0.4
A1	7.7×10^{-7}	0.16	-	-	-
A2	7.7×10^{-6}	0.05	-	-	-
A3	7.7×10^{-5}	0.65	0.31	52	3.4
A4	1.9×10^{-4}	0.68	0.19	72	4.9
A5	3.8×10^{-4}	0.67	0.14	79	5.3
B1	7.8×10^{-7}	0.20	-	-	-
B2	7.8×10^{-6}	0.09	-	-	-
B3	7.7×10^{-5}	0.53	0.17	67	3.6
B4	1.9×10^{-4}	0.57	0.19	66	3.8
B5	3.9×10^{-4}	0.61	0.11	81	5.0
A6	7.7×10^{-7}	0.05	0.005	88	0.4
A7	7.7×10^{-6}	0.09	0.05	52	0.5
B6	7.8×10^{-7}	0.11	0.03	75	0.8
B7	7.8×10^{-6}	0.09	0.03	67	0.6

Thus, when excluding experiments with low N_c, the highest percentage of recovered hydrogen is 81% for exp. B5. The roughly 20% of trapped and dissolved hydrogen is an amount typically associated when gas is being displaced by water (Carden & Paterson, 1979). Similar numbers have also been observed recently in the *Underground Sun Storage* (USS) project by RAG Austria in Vöcklarbruck, Austria (Pichler, 2019). During their first field pilot, 115,444 Nm³ hydrogen was injected into a depleted gas reservoir, of which 94,549 Nm³ were withdrawn, giving a recovery of 82%. The salinity of the reservoir is considered low (0.2 mol/kgw) but the wettability is not defined speficially. Generally, however, gas reservoirs are assumed to be water-wet, except for deeper reservoirs, where oil may have been generated first and then transformed to gas due to pressure and temperature change (Desbrandes & Bassiouni, 1990). With a depth of 1,022 meters, the reservoir of the USS lies outside the typical depth of oil generation (2000-5500 meters)(Malyshev, 2013). Thus, the conditions of the depleted gas reservoir of the USS can be compared to that of an aquifer. However, in their first pilot project,

the injected gas consisted of only 10% hydrogen and 90% methane. A pure hydrogen injection project is under planning by the RAG and is expected to launch in the next few years.

Results in Table 3.4 would typically, however, only be categorized as the first cycle of hydrogen storage and withdrawal. Historically, UHS facilities may run one to three cycles per year which, depending on the lifetime of the reservoir, results in around 60-100 total cycles (Zivar, Kumar, & Foroozesh, 2021). During this study, an attempt at multiple drainages and imbibition cycles was made but deemed unsuccessful (see Table 3.5). In exp. C1, 100 PV primary drainage was conducted equivalent to the 14 previous experiments. Then water was injected until S_{gr} was reached and stopped immediately (i.e.: before any dissolution may occur). Approximately 10 seconds afterward, 100 PV secondary drainage of hydrogen was executed until S_{2g}, followed by secondary water imbibition until S_{2gr} was reached. These procedures were performed in a total of 3 cycles.

Table 3.5. Recovery percentage during three cycles of hydrogen drainage and imbibition.

		1st cycle			2nd cycle			3rd cycle		
Exp. #	N_c ±0.3	S_g	S_{gr}	[%]	S_{2g}	S_{2gr}	[%]	S_{3g}	S_{3gr}	[%]
C1	7.7×10^{-5}	0.48	0.11	56	0.51	0.31	40	0.23	0.34	-28

Although the first and second cycles show reasonable numbers, the major deviation is the negative 28% production of hydrogen during the last cycle. That percentage indicates that there was no gas reduction during water imbibition from S_{3g} to S_{3gr}, but instead, hydrogen saturation increased from 23% to 34%. Because we are only observing a specific section located at the upper right part of the micromodel, the additional hydrogen during the last cycle must have been displaced by the injected water from other parts of the micromodel and into the observed field of view. Despite the poor quantitative data, there was still made a qualitative observation

for the hydrogen cycles: during the three cycles, the same cluster of hydrogen was seen during both drainage and imbibition (see Figure 3.15), indicating that some of the residual trapped hydrogen for each cycle was the same throughout and not replenished. Specifically, this means that some of the initially trapped hydrogen will remain so through multiple cycles and is unable to be produced by neither primary-, secondary, nor tertiary imbibition.
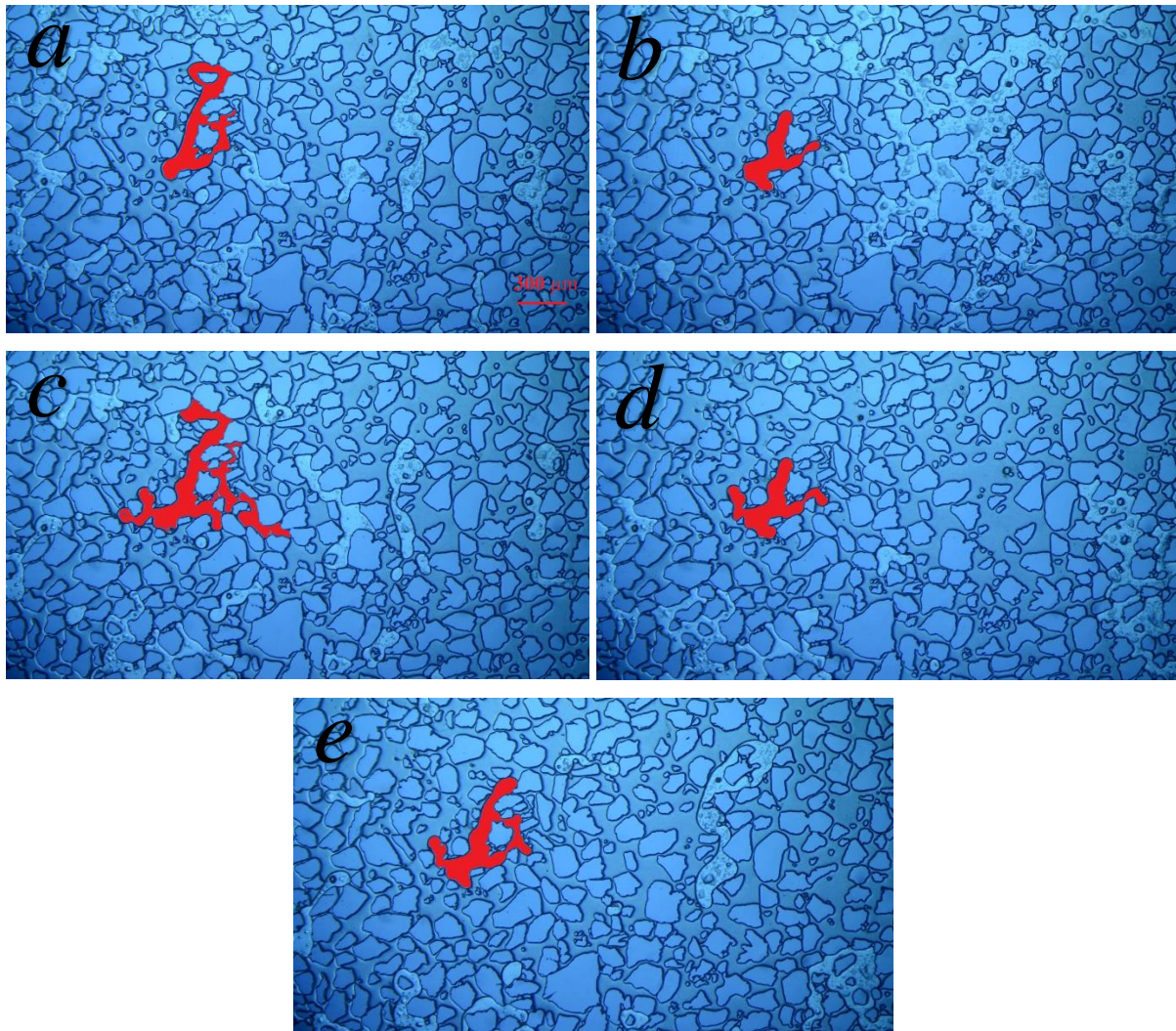
Figure 3.15. Hydrogen saturation through three injection and withdrawal cycles. The red area indicates a hydrogen cluster that remains unproduced throughout all cycles until dissolution occurred. **a** *Primary drainage.* **b** *Secondary drainage.* **c** *Secondary imbibition.* **d** *Tertiary drainage.* **e** *Tertiary imbibition.*

For future work with hydrogen cycle analysis, it is recommended to use a full field of view, in addition to having an outlet for the recovered hydrogen during each cycle. These precautions will give an improved overview of the process, as well as avoid having recycled hydrogen after each cycle. Not only the attempt at cycling hydrogen injection and withdrawal but also results involving hydrogen saturation at low N_c have shown increased uncertainty throughout this study (see S_g in section 3.2.1 and C/C_e in section 3.3.4 at $N_c = 7.7 \times 10^{-7}$ -7.7×10^{-6}). When conducting experiments linked to new studies like UHS, there is always a risk of contradictory results. Nevertheless, instead of discarding these results, they were analyzed thoroughly and kept as part of the discussion and improvement for future work.

4 Conclusion

Hydrogen drainage and distilled water imbibition utilizing a micromodel were investigated both qualitatively and quantitatively. This chapter presents key observations and is divided into three main groups: fluid saturations, hydrogen trapping mechanisms, and hydrogen dissolution and solubility.

Fluid Saturations

- During drainage, hydrogen saturation in the water-saturated micromodel increased with capillary number until a specific water saturation was reached. This water saturation could not be lowered by a further increase in capillary number, thus an irreducible water saturation of the micromodel was found.

- Experiments showed no change in hydrogen saturation between gas breakthrough and an additional 100 pore volume of hydrogen injected, thus indicating the bypassing of water.

- Due to the stochasticity of pore-scale displacement, experiments with the lowest capillary numbers showed the highest uncertainty in hydrogen saturation.

Hydrogen trapping mechanisms

- During water imbibition after drainage, hydrogen was observed to be swept out by the injected water until a reduced hydrogen saturation was reached.

- The reduced hydrogen saturation was trapped by both I1 and I2 snap-off, and bypassed by further water injection. Due to the high capillary numbers chosen for this study, I2 snap-off was dominant throughout the experiments, and I1 snap-off was only observed at the lowest capillary number.

Hydrogen dissolution and solubility

- Dissolution of hydrogen was mainly driven by advection at the water-hydrogen interface. A small dissolution by diffusion was only observed at the lowest capillary number during the initial imbibition until the reduced hydrogen saturation was reached.

- An increase in capillary number and pressure inside the micromodel resulted in a faster dissolution and higher depletion rate.

- For individual hydrogen bubbles and clusters, both homogeneous and heterogeneous dissolution was observed. Heterogeneous dissolution was dominant throughout every

experiment and capillary number, and homogeneous dissolution was seen infrequently at low and medium capillary numbers.

- Depletion rates of individual hydrogen bubbles and clusters were influenced by the changing water-hydrogen interface. A declining depletion rate was observed for hydrogen bubbles, whereas clusters had highly oscillating depletion rates with seemingly random patterns.

- The solubility of hydrogen in water was slightly dependent on the capillary number of the injected phase and highly dependent on the pressure inside the micromodel.

- Dissolution as a function of injected pore volume during imbibition has shown higher effectiveness at lower capillary numbers, i.e., more dissolution per mass volume of injected water. This may have been supported by the solubility concentration of hydrogen bubbles at lower capillary numbers being closer to equilibrium solubility. However, under various experimental conditions, equilibrium solubility was never achieved because of the limited water-hydrogen interface available for advection and limited resident time.

5 Future work

During this thesis, some observations were made for improvement and future work.

- Generally, a field of view of the entire micromodel would increase the accuracy of all conducted experiments, especially the solubility of hydrogen in water and fluid saturations at lower capillary numbers.

- The use of dyed water or fluorescent tracers during experiments would mitigate the need for editing software such as Paint 3-D to map fluid saturations, and thus reduce the work hours significantly. It would also increase the overall accuracy of the measured fluid saturations.

- Modifications of the experimental setup to enable hydrogen cycle experiments and investigate the effect on hysteresis.

- The use of brine to investigate the effect of salinity on hydrogen solubility in water.

- Cushion gas has been used to maintain the pressure in depleted reservoirs, thus experiments with hydrogen, methane, and/or nitrogen mixture would be of interest.

- To investigate the effect of dissolution by diffusion, experiments with lower capillary numbers are needed. Due to leakage from valves and tubing, the current experimental setup is not designed to conduct experiments at capillary numbers lower than 7×10^{-7}.

6 Appendix

6.1 Uncertainties

This section will give a summary of uncertainties in the conducted experiments during this thesis.

Every result obtained during this study was based on image analysis on fluid saturations. To calculate the uncertainty in fluid saturation mapping, some images were edited three times and the deviation from the mean value was used. In section 3.2, the assumption was made that due to the repeated pore networks, the fluid saturation of the field of view can be applied to the whole micromodel. Thus, at different capillary numbers, the fluid saturation of different field-of-views was measured and the deviation from the mean value was used as additional uncertainty for the individual experiments. The standard deviation for a sample set of data was thus calculated as follows:

$$S = \sqrt{\frac{\sum_{i=1}^{n}(x_i - \bar{x})^2}{n-1}}$$

where x_i is each value of the data set, $\bar{x}$ is the mean value of all data sets, and n is the number of values in the data set. The Quizix 5200 pump system has an uncertainty of 0.2% of the injection rate (Folkvord, 2020), and 0.2% of the max-rated pressure (Iden, 2017). The uncertainty of the injection rate was further used for Darcy velocity and capillary number calculations. Due to the difference but also utmost importance for this thesis, the uncertainties of dissolution, depletion rates, and solubility were not listed in tables, but rather discussed throughout chapter 3. Dissolution and imbibition times were calculated directly from video or interval pictures without the use of a timer, thus, no quantitative uncertainties were measured. However, because videos required a manual restart every 30 minutes, there was an estimated 10 second (0.2 min) deviation in how long this restart on average would take.

6.2 Nomenclature

θ_a	Advancing angle	[˚]
θ_g	Gas contact angle	[˚]
θ_r	Receding angle	[˚]
σ	Interfacial tension	[nM/m]
φ	Porosity	-
φ_l	Local porosity	-
μ_n	Viscosity of the native fluid	[pa $\times$ s]
A_g	Area of grains	[pixel]
A_h	Area of hydrogen	[pixel]
A_p	Area of pores	[pixel]
A_t	Total image area	[pixel]
C	Solubility of H_2 in H_2O	[kg/mol]
C_e	Equilibrium solubility of H_2 in H_2O	[kg/mol]
C_c	Solubility concentration of H_2 in H_2O	[kg/mol]
F_v	Viscous force	[Newton]
J	Diffusion flux	[kg/Area]
m	Salinity;NaCl per kg water	[mol/kgw]
n	Refractive index	-
N_c	Capillary Number	-
P_c	Capillary pressure	[bar]
P_c^e	Capillary entry pressure	[bar]
Q	Injection rate	[mL/h]
Q_d	Depletion rate	[gram/sec]
S_{wi}	Irreducible water saturation	-
S_g	Hydrogen gas saturation	-
S_{gr}	Reduced gas saturation	-
S_w	Water saturation	-
t_d	Total dissolution time	[sec]
v_d	Darcy velocity	[m/s]
V_p	Pore volume	[mL]
V_r	Recovered hydrogen	[μL]

6.3 Abbreviations

CCS	Carbon capture and storage
CDC	Capillary Desaturation Curve
CH_4	Methane
CO	Carbon monoxide
CO_2	Carbon dioxide
DRIE	Deep Reactive Ionic Etching
H_2	Hydrogen
N_2	Nitrogen
N_2	Nitrogen
PD	Primary drainage
PEEK	Polyether ether ketone
SD	Secondary drainage
SDG	Sustainable development goal
SMR	Steam methane reforming
TD	Tertiary drainage
TWh	Terawatt hours
UHS	Underground hydrogen storage
USS	Underground Sun Storage

6.4 Bibliography

Alley, W. M., Reilly, T. E., & Franke, O. L. (1999). *Sustainability of ground-water resources* (Vol. 1186): US Department of the Interior, US Geological Survey.

Amigáň, P., Greksák, M., Kozánková, J., Buzek, F., Onderka, V., & Wolf, I. (1990). Methanogenic bacteria as a key factor involved in changes of town gas stored in an underground reservoir. *FEMS Microbiology Ecology, 6*(3), 221-224. doi:10.1111/j.1574-6968.1990.tb03944.x

Azretovna Abukova, L., Nabievich Zakirov, S., Pavlovich Anikeev, D., & Sumbatovich Zakirov, E. (2020). *Formation of an Effective Hydrogen Storage in an Aquifer and Control of its Parameters.* Paper presented at the SPE Russian Petroleum Technology Conference.

Benali. (2019). Quantitative Pore-Scale Analysis of CO2 Foam for CCUS.

Bruun, J., Graf, T., Iskov, H., & Koch, B. (2014). Energy Storage–Hydrogen injected into the Gas Grid via electrolysis field test. In: Fredericia.

Buchgraber, M., Kovscek, A. R., & Castanier, L. M. (2012). A Study of Microscale Gas Trapping Using Etched Silicon Micromodels. *Transport in Porous Media, 95*(3), 647-668. doi:10.1007/s11242-012-0067-0

Carden, P. O., & Paterson, L. (1979). Physical, chemical and energy aspects of underground hydrogen storage. *International Journal of Hydrogen Energy, 4*(6), 559-569. doi:https://doi.org/10.1016/0360-3199(79)90083-1

Chabab, S., Théveneau, P., Coquelet, C., Corvisier, J., & Paricaud, P. (2020). Measurements and predictive models of high-pressure H2 solubility in brine (H2O+NaCl) for underground hydrogen storage application. *International Journal of Hydrogen Energy, 45*(56), 32206-32220. doi:https://doi.org/10.1016/j.ijhydene.2020.08.192

Chang, C., Zhou, Q., Kneafsey, T. J., Oostrom, M., & Ju, Y. (2019). Coupled supercritical CO2 dissolution and water flow in pore-scale micromodels. *Advances in Water Resources, 123*, 54-69. doi:https://doi.org/10.1016/j.advwatres.2018.11.004

Chang, C., Zhou, Q., Kneafsey, T. J., Oostrom, M., Wietsma, T. W., & Yu, Q. (2016). Pore-scale supercritical CO2 dissolution and mass transfer under imbibition conditions. *Advances in Water Resources, 92*, 142-158. doi:https://doi.org/10.1016/j.advwatres.2016.03.015

Dannevig, P., & Harstveit, K. (2021). klima i Norge. [climate in Norway]. *SNL.* Retrieved from https://snl.no/klima_i_Norge

de Montety, V., Radakovitch, O., Vallet-Coulomb, C., Blavoux, B., Hermitte, D., & Valles, V. (2008). Origin of groundwater salinity and hydrogeochemical processes in a confined coastal aquifer: Case of the Rhône delta (Southern France). *Applied Geochemistry, 23*(8), 2337-2349. doi:https://doi.org/10.1016/j.apgeochem.2008.03.011

Desbrandes, R., & Bassiouni, Z. A. (1990). In-Situ Wettability Determination in Gas Reservoirs. *SPE Formation Evaluation, 5*(04), 431-436. doi:10.2118/19058-pa

Deutsche Welle, E. b. f. h. w. a. e. p. s. h. h. (2021). Europeans brace for hard winter as energy price surge hits households. Retrieved from https://www.dw.com/en/europeans-brace-for-hard-winter-as-energy-price-surge-hits-households/a-59246714

Ding, M., & Kantzas, A. (2007). Capillary Number Correlations for Gas-Liquid Systems. *Journal of Canadian Petroleum Technology, 46*(02). doi:10.2118/07-02-03

Dr.Jawad.Alassal, Yahya Jirjees, A., Mohamedali, S., Sajad, S., & Namiq, M. (2017). *Reservoir engineering handbook.*

Folkvord. (2020). Applying in-situ imaging and streamtube analysis to quantify carbonate dissolution at the core scale – an experimental study applying positron emission tomography (PET) and computed tomography (CT).

Hale, G. M., & Querry, M. R. (1973). Optical Constants of Water in the 200-nm to 200-μm Wavelength Region. *Applied Optics, 12*(3), 555-563. doi:10.1364/AO.12.000555

Hornbrook, J. W., Castanier, L. M., & Pettit, P. A. (1991). *Observation of Foam/Oil Interactions in a New, High-Resolution Micromodel.* Paper presented at the SPE Annual Technical Conference and Exhibition.

Iden, E. J. (2017). *Pore-Level Interpretation of Methane Hydrate Growth and Dissociation with Deionized and Saline Water.* The University of Bergen,

IRENA. (2018). Retrieved from https://www.irena.org/-/media/Files/IRENA/Agency/Publication/2018/Sep/IRENA_Hydrogen_from_renewable_power_2018.pdf

Jiang, G., Li, Y., & Zhang, M. (2013). Evaluation of gas wettability and its effects on fluid distribution and fluid flow in porous media. *Petroleum Science, 10*(4), 515-527.

Jin, J., Kim, J. W., Kang, C.-S., Kim, J.-A., & Eom, T. B. (2010). Thickness and refractive index measurement of a silicon wafer based on an optical comb. *Optics Express, 18*(17), 18339-18346. doi:10.1364/OE.18.018339

Katsutoshi Ono. (2014). Fundamental Theories on a Combined Energy Cycle of an Electrostatic Induction Hydrogen Electrolytic Cell and Fuel Cell to Produce Fully Sustainable Hydrogen Energy. doi:10.1002

Lee, M. C., Seo, S. B., Yoon, J., Kim, M., & Yoon, Y. (2012). Experimental study on the effect of N2, CO2, and steam dilution on the combustion performance of H2 and CO synthetic gas in an industrial gas turbine. *Fuel, 102*, 431-438. doi:https://doi.org/10.1016/j.fuel.2012.05.028

Lenormand, R., & Zarcone, C. (1984). *Role Of Roughness And Edges During Imbibition In Square Capillaries.* Paper presented at the SPE Annual Technical Conference and Exhibition.

Lien. (2004). Grunnlegende Reservoarfysikk (Kjerneanalyse og logging).

Lord, A. S., Kobos, P. H., Klise, G. T., & Borns, D. J. (2011). A life cycle cost analysis framework for geologic storage of hydrogen: a user's tool. *Sandia Report (SAND2011-6221) Sandia National Laboratories (Sep. 2011), 60*.

Lysyy. (2018). Pore-scale investigation of methane hydrate phase transitions and growth rates in synthetic porous media.

Malyshev. (2013). Origin of Oil. Retrieved from http://large.stanford.edu/courses/2013/ph240/malyshev2/

Marshak, S. (2011). *Earth: Portrait of a Planet: Fourth International Student Edition*: WW Norton & Company.

Mohsenatabar Firozjaii, A., Derakhshan, A., & Shadizadeh, S. R. (2018). An investigation into surfactant flooding and alkaline-surfactant-polymer flooding for enhancing oil recovery from carbonate reservoirs: Experimental study and simulation. *Energy Sources, Part A: Recovery, Utilization, and Environmental Effects, 40*(24), 2974-2985.

NVE. (2021). Kraftproduksjon. Retrieved from https://www.nve.no/energiforsyning/kraftproduksjon/

Peck, E. R., & Huang, S. (1977). Refractivity and dispersion of hydrogen in the visible and near infrared. *Journal of the Optical Society of America, 67*(11), 1550-1554. doi:10.1364/JOSA.67.001550

Pfeiffer, W. T., Beyer, C., & Bauer, S. (2017). Hydrogen storage in a heterogeneous sandstone formation: dimensioning and induced hydraulic effects. *Petroleum Geoscience, 23*(3), 315-326. doi:10.1144/petgeo2016-050

Pichler, M. (2019). *Underground Sun Storage Results and Outlook.* Paper presented at the EAGE/DGMK Joint Workshop on Underground Storage of Hydrogen.

Polyanskiy. (2021). Refractive index database Retrieved from https://refractiveindex.info/?shelf=glass&book=HIKARI-BK&page=J-BK7A

Rossen, W. R. (2000). Snap-off in constricted tubes and porous media. *Colloids and Surfaces A: Physicochemical and Engineering Aspects, 166*(1), 101-107. doi:https://doi.org/10.1016/S0927-7757(99)00408-2

Rowlat, J. (2021). Why electric cars will take over sooner than you think. *BBC*. Retrieved from https://www.bbc.com/news/business-57253947

Saga, S. (2021). Mechanical Sensors. In *Reference Module in Biomedical Sciences*: Elsevier.

Sandnes, M. F. (2020). *Wetting Stability of Aged Limestone in the presence of HPAM polymer.* The University of Bergen,

The Engineering Toolbox. (2021). Solubility of Gases in Water. Retrieved from https://www.engineeringtoolbox.com/gases-solubility-water-d_1148.html#google_vignette

The World Of Hydrogen. (2021). What is hydrogen and how is it made? Retrieved from https://www.theworldofhydrogen.com/gasunie/what-is-hydrogen/

Tweheyo, M., Talukdar, M., & Torsæter, O. (2001). *Hysteresis effects in capillary pressure, relative permeability and resistivity index of north sea chalk.* Paper presented at the Paper SCA 2001-65 presented at the International Symposium of the Society of Core Analysts held in Edinburgh, UK.

USP. (2015). General Notices, Requirements USP< 38>. *United States Pharmacopeia*. Retrieved from https://www.uspnf.com/sites/default/files/usp_pdf/EN/USPNF/usp-nf-notices/usp38_nf33_gn.pdf

Yeganeh, M., Hegner, J., Lewandowski, E., Mohan, A., Lake, L. W., Cherney, D., . . . Jaishankar, A. (2016). *Capillary Desaturation Curve Fundamentals.* Paper presented at the SPE Improved Oil Recovery Conference.

Yekta, A. E., Manceau, J. C., Gaboreau, S., Pichavant, M., & Audigane, P. (2018). Determination of Hydrogen–Water Relative Permeability and Capillary Pressure in Sandstone: Application to Underground Hydrogen Injection in Sedimentary Formations. *Transport in Porous Media, 122*(2), 333-356. doi:10.1007/s11242-018-1004-7

Zhang, D. (2001). *Stochastic methods for flow in porous media: coping with uncertainties*: Elsevier.

Zivar, D., Kumar, S., & Foroozesh, J. (2021). Underground hydrogen storage: A comprehensive review. *International Journal of Hydrogen Energy, 46*(45), 23436-23462.

Zolotuchin, A. B. (2000). *Introduction to petroleum reservoir engineering*. Kristiansand: Høyskoleforl.

Zolotukhin, A. B., & Ursin, J.-R. (2000). *Introduction to petroleum reservoir engineering*: Norwegian Academic Press.